NANO · MICRO
small

Supporting Information

for *Small*, DOI 10.1002/smll.202404297

A Super-Ionic Solid-State Block Copolymer Electrolyte

Daniel T. Krause, Beate Förster, Martin Dulle, Susanna Krämer, Steffen Böckmann, Caroline Mönich, Michael Ryan Hansen, Monika Schönhoff, Vassilios Siozios, Mariano Grünebaum, Martin Winter, Stephan Förster and Hans-Dieter Wiemhöfer**

SUPPORTING INFORMATION

A Super-ionic Solid-state Block Copolymer Electrolyte

Daniel T. Krause, Beate Förster, Martin Dulle, Susanna Krämer, Steffen Böckmann, Caroline Mönich, Michael Ryan Hansen, Monika Schönhoff, Vassilios Siozios, Mariano Grünebaum, Martin Winter, Stephan Förster, Hans-Dieter Wiemhöfer**

D. T. Krause, S. Krämer, M. Grünebaum, M. Winter, H.-D. Wiemhöfer
Helmholtz Institute Münster, IEK-12, Forschungszentrum Jülich GmbH, Corrensstr. 46, 48149 Münster, Germany
E-mail: D. T. Krause: d_krau05@uni-muenster.de
S. Krämer: su.kraemer@fz-juelich.de
M. Grünebaum: m.gruenebaum@fz-juelich.de
M. Winter: m.winter@fz-juelich.de
H.-D. Wiemhöfer: hdw@uni-muenster.de

B. Förster
Ernst Ruska-Centre for Microscopy and Spectroscopy with Electrons, Physics of Nanoscale Systems (ER-C-1), Forschungszentrum Jülich, Wilhelm-Johnen-Straße, Jülich 52425, Germany
E-mail: B. Förster: b.foerster@fz-juelich.de

M. Dulle, S. Förster
Jülich Centre for Neutron Science (JCNS-1/IBI-8), Forschungszentrum Jülich, Wilhelm-Johnen-Straße, 52425 Jülich, Germany
E-mail: M. Dulle: m.dulle@fz-juelich.de
S. Förster: s.foerster@fz-juelich.de

S. Böckmann, C. Mönich, M. R. Hansen, M. Schönhoff
Institute of Physical Chemistry, University of Münster, Corrensstr. 28/30, 48149 Münster, Germany
E-mail: S. Böckmann: steffen.boeckmann@uni-muenster.de
C. Mönich: c_moen07@uni-muenster.de
M. R. Hansen: mhansen@uni-muenster.de
M. Schönhoff: schoenho@uni-muenster.de

V. Siozios, M. Winter, H.-D. Wiemhöfer
MEET Battery Research Center, University of Münster, Corrensstr. 46, 48149 Münster, Germany
E-mail: V. Siozios: vassilios.siozios@uni-muenster.de

S. Förster
Institute of Physical Chemistry, RWTH Aachen University, Landoltweg 2, 52074 Aachen, Germany

Table of Contents

Synthesis of $PI_xPS_yPEO_{1.9}$ BCPs

The synthesis method for the $PI_xPS_yPEO_{1.9}$ BCPs used here is described and discussed in detail in ref. [21]; in the following, it is only briefly described.

According to our convergent synthesis method, first the PI_x and then the PS_y block is built up by a living sequential anionic polymerization. Finally, $PEO_{1.9}$ chains functionalized with glycidyl end-groups are used to attach the $PEO_{1.9}$ block and to complete the synthesis of $PI_xPS_yPEO_{1.9}$ BCPs simultaneously. The entire $PEO_{1.9}$ end-group modification reaction and polymer synthesis reaction of the $PI_xPS_yPEO_{1.9}$ BCPs were carried out at room temperature in a glovebox under argon atmosphere.

To modify the $PEO_{1.9}$ end-group, sodium *tert*-butoxide (1.5 equiv) was dissolved in THF and added to the solution of $PEO_{1.9}$ (1.0 equiv) in THF. After 72 h, epichlorohydrin (8.0 equiv) was added dropwise within 15 min to the reaction solution and stirred for six days. Subsequently, the solid residue was removed and the product was dissolved in toluene and precipitated in diethyl ether, dissolved again in toluene and reprecipitated three times in diethyl ether. The resulting epoxide end-group modified $PEO_{1.9}$ has been dried at 30 °C in vacuum $<1\cdot10^{-6}$ mbar.

To synthesize the $PI_xPS_yPEO_{1.9}$ BCPs, initially the PI_x was built up, for which the isoprene monomers ($PI_{14.6}PS_{34.8}PEO_{1.9}$: 213.6 equiv, $PI_{26.1}PS_{67.3}PEO_{1.9}$: 383.5 equiv) were dissolved in toluene, then the initiator 1.4 M *sec*-butyllithium solution in cyclohexane (1.0 equiv) was added, and the reaction solution was stirred for 24 h. Subsequently, the PS_y block was synthesized to the living PI_x^- anion by adding the styrene monomers ($PI_{14.6}PS_{34.8}PEO_{1.9}$: 334.1 equiv, $PI_{26.1}PS_{67.3}PEO_{1.9}$: 645.8 equiv), and stirring the reaction solution for 24 h. Finally, the epoxide end-group modified $PEO_{1.9}$ (1.1 equiv) was added to the reaction solution of the living $PI_xPS_y^-$ anion, and stirred for further 48 h to attach the $PEO_{1.9}$ block. Afterwards, 0.5 M hydrogen chloride solution in methanol (1.5 equiv) was added, all volatile components were removed at 40 °C under vacuum, followed by dissolution of the product in dichloromethane, precipitation in methanol, and this procedure was repeated three times. The resulting $PI_xPS_yPEO_{1.9}$ BCPs have been dried at 50 °C in vacuum $<1\cdot10^{-6}$ mbar.

Optical Observation of Neat BCP and SPE Membranes and LiTFSI/THF Residue

Even at the smallest $[Li^+:O_{EO}]_n$ of 1.0:1, the colorless and transparent neat BCP membranes become white and non-transparent SPE membranes due to the embedding of the LiTFSI. After the casting process, when the SPE membranes were removed from the crucibles, varying amounts of a viscous, colorless, and transparent residue of LiTFSI/THF was still inside the crucibles (Fig. S1). The amount of LiTFSI/THF residue increased with higher $[Li^+:O_{EO}]_n$. This implies that not all of the intended LiTFSI amount was incorporated into the SPE membrane during the casting process, but remained in the crucible as LiTFSI/THF residue. Therefore, especially when the LiTFSI saturation limit is reached at $[Li^+:O_{EO}]_n \geq 3.1:1$, macroscopic phase separation is observed, forming an SPE membrane phase and a liquid LiTFSI/THF phase.

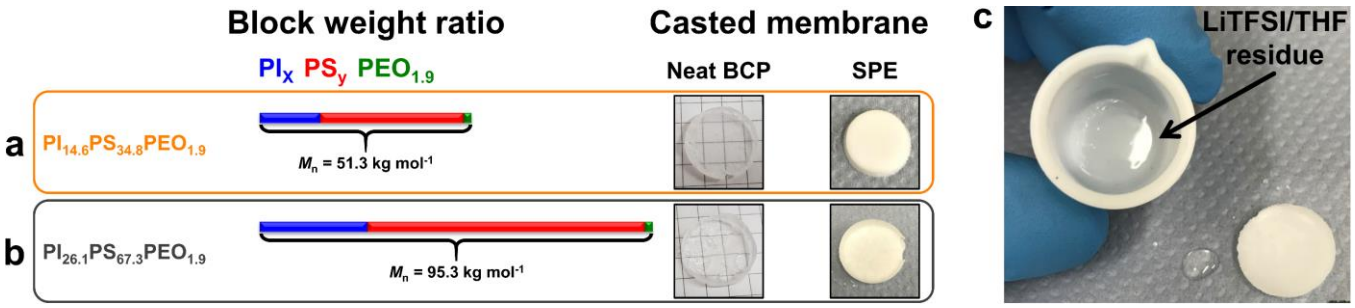

Fig. S1 | Polymer chain length overview of each block and photos of neat BCP and SPE membrane as well as the LiTFSI/THF residue. In **a**, and **b**, the polymer chain length of each block is shown relative to the M_n, as well as an optical comparison based on photos of the neat BCP and the corresponding SPE membranes. In **c**, a crucible after the casting process containing the LiTFSI/THF residue after removal of the SPE membranes is depicted.

^{19}F-NMR and LiTFSI Saturation Limit

Sample preparation: The SPE membrane and the ^{19}F-atom containing internal standard were precisely weighed. For solid state NMR measurements, polytetrafluoroethylene (PTFE) tape (DIN EN 715-3) was used as the external standard because its ^{19}F-signal relaxation is adequately fast. For solution-NMR, bis(fluorosulfonyl)imide lithium salt (LiFSI) was chosen as appropriate standard because it is well soluble in THF and the chemical shift of its ^{19}F-signal is sufficiently far away from that of LiTFSI so that no signal overlap occurs. Due to the hygroscopic nature of LiTFSI, the entire sample preparation was done under exclusion of humidity. Therefore, solid-state NMR rotors were packed in a dry room (dew point <-66 °C), and for liquid NMR measurements, solutions were prepared in THF and filled into NMR tubes under argon atmosphere inside a glovebox. Care was taken during weighing of the SPE membrane and the internal standard to ensure that the concentration of fluorine atoms between both did not differ by more than a factor of three, so that their signal intensity ratio in

the obtained ^{19}F-NMR spectrum was as equal as possible. For this purpose, each weighed sample's mass, but also the number of ^{19}F-atoms contained per molecule, were considered. LiTFSI and LiFSI are both symmetric molecules, with LiTFSI having two CF_3-groups and thus six identical ^{19}F-atoms, whereas LiFSI has only two identical ^{19}F-atoms because it has two single F-atom groups, so that the LiTFSI molecule contains three times more ^{19}F-atoms.

Measurement set-up: ^{19}F-solution-NMR spectra of all SPEs were recorded at 30 °C using a Benchtop Spinsolve 80 MHz (Magritek). NMR measurements with a number of scans = 4096 or 8192 were recorded, using an acquisition time of 0.41 s and a repetition time of 8 s, to ensure a good signal-to-noise ratio, and consequently a good quantification of both ^{19}F-signals. The spectra were analyzed with the software MestReNova (version: 12.0.4-22023, Mestrelab Research).

Quantitative solid-state ^{19}F MAS NMR spectra were acquired on a Bruker Avance Neo console operating at a static field of 11.76 T ($\nu_L(^{19}F)$ = 470.80 MHz) using a commercial Bruker 4 mm H/F/X MAS DVT probe equipped with magic-angle gradient coils. All measurements were performed at 12.5 kHz MAS using dry N_2 as driving gas and at ambient temperature. The magic angle was calibrated prior to the measurements by optimizing the spinning-sideband intensity in the ^{23}Na spectrum of solid $NaNO_3$ spinning at 5 kHz. The quantification was done *via* the ^{19}F signal in a simple single pulse-experiment using PTFE tape (DIN EN 751-3) as an external reference sample for the replacement method. From the total ^{19}F signal intensity of the PTFE reference spectrum and its known ^{19}F spin density (0.03999 mol g^{-1}), the ^{19}F spin density of an SPE sample and, hence, the LiTFSI content can be calculated using the ^{19}F signal intensity of the SPE sample and the spin density of pure LiTFSI (0.02090 mol g^{-1}). Special care was taken to keep the experimental conditions identical between the measurement of the PTFE reference sample and the membrane samples. The PTFE reference sample and the SPE samples were packed identically (without any spacer material to ensure identical effects like inhomogeneous B_1 fields of the r.f. coil) in identical rotors (4 mm thick wall rotors, i.d. 3 mm) to minimize susceptibility effects and, hence, the necessary rematching and -tuning of the probe after sample change. Also, the spectra were acquired using the same receiver dead-time, dwell-time, receiver gain and irradiation frequency as these all influence the absolute intensity of the signal acquired with a digital receiver. Spectra of the PTFE reference and SPE membrane samples were acquired directly after one another. The longitudinal relaxation time T_1 was estimated for the PTFE reference and every SPE sample using a coarse saturation-recovery experiment with relaxation delays spaced by a factor of 2 from 0.5 s to 32 s. For all SPE samples full relaxation was usually achieved after a relaxation delay of 4 s. The relaxation delay was then chosen to ensure full longitudinal relaxation, which was 32 s for the SPE samples and 128 s for the PTFE reference. A 90° excitation pulse with a length of 4.2 μs was used in all single-pulse experiment and found to have a

sufficient uniform excitation bandwidth for both, the reference and SPE membrane samples. Although the pulse length was re-optimized for maximum signal intensity for every sample, no notable deviations from this value were observed and, hence, no adjustments were necessary. Finally, all spectra were identically processed, and a manual baseline correction was performed several times for every spectrum to estimate errors that may arise from fitting the baseline differently. The total signal intensity is then simply given by the integral over the spectra and proportional to the number of spins in the active volume.

Additional information: We chose the ^{19}F-atom for LiTFSI quantification because it can be selectively attributed solely to the LiTFSI in the SPE membranes as it is otherwise not present in the SPE, which makes it most suitable for quantification. As a result of the sample preparation and the selected instrument settings, the amount of LiTFSI embedded in the SPE membrane was quantified by its ^{19}F-atomic quantity relative to LiFSI or PTFE as an internal standard using ^{19}F-NMR measurements.

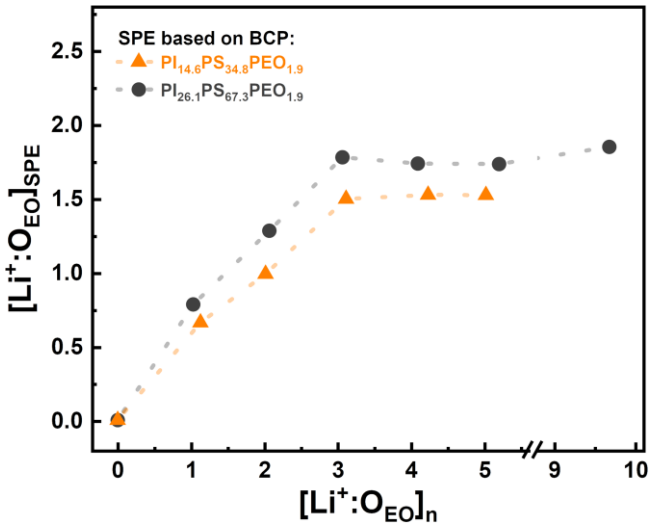

Fig. S2 | LiTFSI amount embedded in the PEO phase ($[Li^+:O_{EO}]_{SPE}$) depending on the added LiTFSI content ($[Li^+:O_{EO}]_n$). Results of the SPE membranes from both BCPs are shown, where the $[Li^+:O_{EO}]_{SPE}$ was calculated by relating the determined LiTFSI amount (by ^{19}F-solution NMR) to the PEO wt.% of the respective BCP in the SPE. We conclude that the maximum uptake of LiTFSI in the PEO phase is $[Li^+:O_{EO}]_{SPE,sat}$ = 1.5:1 for SPEs from $PI_{14.6}PS_{34.8}PEO_{1.9}$ and 1.9:1 for SPEs from $PI_{26.1}PS_{67.3}PEO_{1.9}$.

Thermogravimetric Analysis (TGA)

Sample preparation: Care was taken to ensure that the samples did not come into contact with air (oxygen and moisture). Therefore, all samples (neat THF, neat LiTFSI, neat BCPs, SPEs, binary LiTFSI/THF mixtures, and ternary LiTFSI/PEO/THF mixture) were prepared in a glovebox under argon atmosphere. ~10 mg of sample was placed into an aluminum pan and hermetically sealed, subsequently loaded into the instrument with no contact with ambient air and punctured inside the furnace under helium atmosphere.

Measurement set-up: The measurement was performed on a TGA-5500 with IR furnace (TA Instruments) under a helium flow through the TGA-balance (balance purge) of 30 mL min^{-1}, a helium flow across the sample of 25 mL min^{-1}, and using a constant heating rate of 2 K min^{-1} in a temperature range of 30 - 600 °C. This high helium flow was used to maximize the vapor pressure of THF, which facilitated its evaporation. The TGA signals were analyzed with the TA Instruments TRIOS software (version: 5.1.1.46572, TA Instruments).

Additional information: For inferring the amount of THF in the SPE membranes from the weight loss obtained by TGA measurements, it was important to ensure that the total amount of THF is evaporated. However, the THF is hindered from evaporating due to the coordination with the embedded LiTFSI, but it has to evaporate before decomposition of the neat BCP and LiTFSI occurs. Otherwise the weight loss caused by the decomposition would be misinterpreted as THF and thus lead to a too high amount. This means that the SPEs must be heated to a sufficiently high temperature as long as possible, but both the temperature and the duration of heating, i.e. the temperature effect, must not be too strong. This challenge was solved by the selected high helium flow and temperature-time profile, which can be found in Fig. S3, in combination with the slow heating rate of 2 K min^{-1}. During this profile, the SPE sample is heated to 200 °C in the 1st heating ramp, then fast cooled down to 30 °C and heated to 600 °C in the subsequent 2nd heating ramp. This is plotted in simplified manner on the upper X-axis for all TGA measurements.

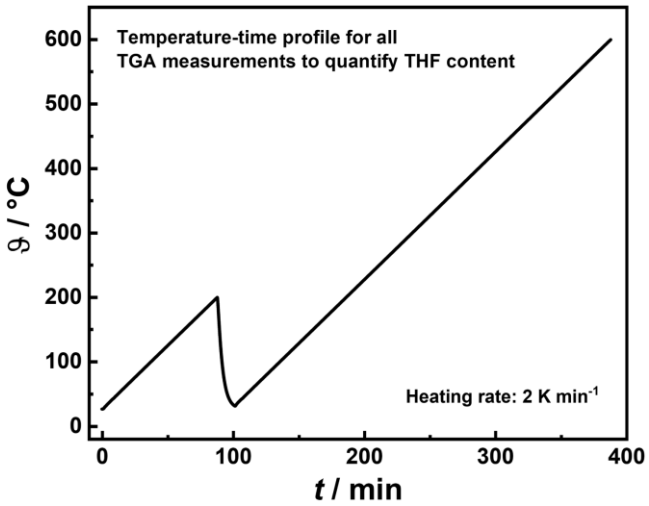

Fig. S3 | Temperature-time profile used for THF content determination of all TGA measurements. During this profile, the SPE sample is heated to 200 °C in the 1st heating ramp, then fast cooled down to 30 °C and heated to 600 °C in the subsequent 2nd heating ramp. For clarity, this profile has not been plotted in the respective TGA measurements; instead, a simplified temperature variation is shown on the upper X-axis.

The high helium flow which is used for mild THF evaporation increases the THF vapor pressure. Consequently, the THF evaporates considerably faster at the same temperature. This can be seen from the TGA measurement of neat THF, as it is already completely vaporized after 3 min, whereas the

temperature was only increased by 5 to 35 °C (Fig. S4). From the measurements of both binary LiTFSI/THF mixtures and the ternary LiTFSI/PEO/THF mixture, it is clear that the combination of the selected temperature-time profile and the high helium flow ensures that all of the THF evaporates up to 280 °C, hence including that coordinated to the LiTFSI. As seen from DSC measurements (Fig. S11), all THF in the binary mixtures of LiTFSI/THF is coordinated to the LiTFSI at a $[Li^+:O_{THF}] \geq 0.25:1$, thus, also in the LiTFSI/THF mixture with $[Li^+:O_{THF}] = 0.61:1$ and in the LiTFSI/PEO/THF mixture with $[Li^+:O_{EO+THF}] = 0.71:1$ from Fig. S4. Nevertheless, the observed mass loss in Fig. S4 corresponds to the used amount of THF, so it is evident that up to 280 °C also all bound THF evaporates.

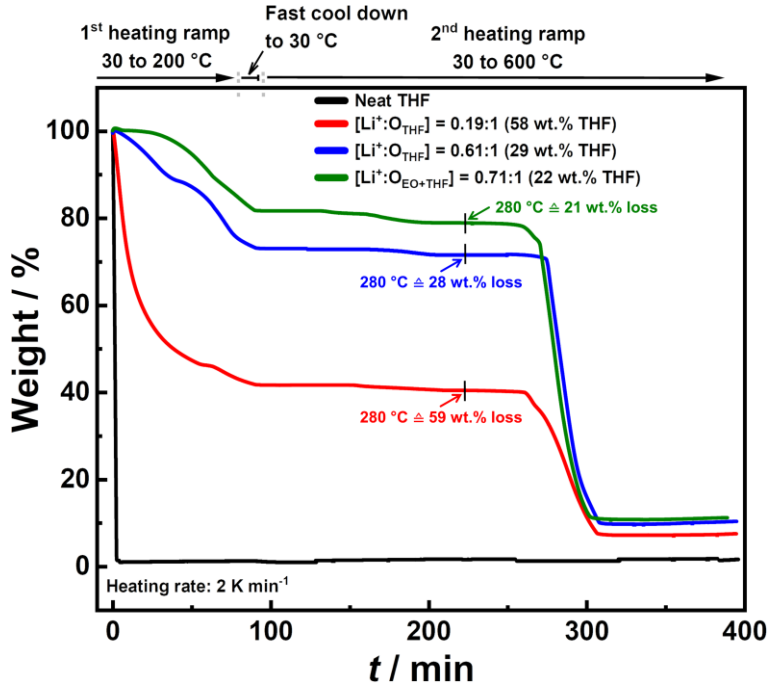

Fig. S4 | Total THF amount, including the one coordinated with LiTFSI, evaporates up to 280 °C. TGA curves of neat THF, two binary LiTFSI/THF mixtures and a ternary LiTFSI/PEO/THF mixture. For a better overview, the weight loss was plotted against time, as the TGA measurements consist of two sequential heating ramps. The temperature profile has been simplified on the upper X-axis and the whole temperature-time profile is shown in Fig. S3. In the ternary mixture, the $[Li^+:O_{EO+THF}]$ refers to the stoichiometric ratio between Li^+ and the O-donor atoms from THF and PEO. The combination of the selected high helium flow and the temperature-time profile ensures that all THF evaporates up to 280 °C, and was therefore used for THF content determination in the SPE membranes.

All SPE membranes show the same weight loss behavior during the TGA measurement, which can be seen in Fig. S5. In the 1st heating ramp, the weight loss is solely attributable to the evaporation of the THF, as it was only heated up to 200 °C and thus no decomposition of the neat BCP and the LiTFSI occurred. In order to evaporate remaining THF, but also to check if there was still THF in the SPE, it was cooled down to 30 °C and heated up again in the 2nd heating ramp. The cooling step minimized thermal stress to avoid decomposition. Almost no further weight loss occurred in the 2nd

heating ramp until decomposition of the neat BCP and LiTFSI starts at around 300 °C. Consequently, the weight loss at 280 °C is completely attributable to the evaporation of THF and was selected as the point for determining the amount of THF for all SPEs, before the decomposition starts at higher temperature.

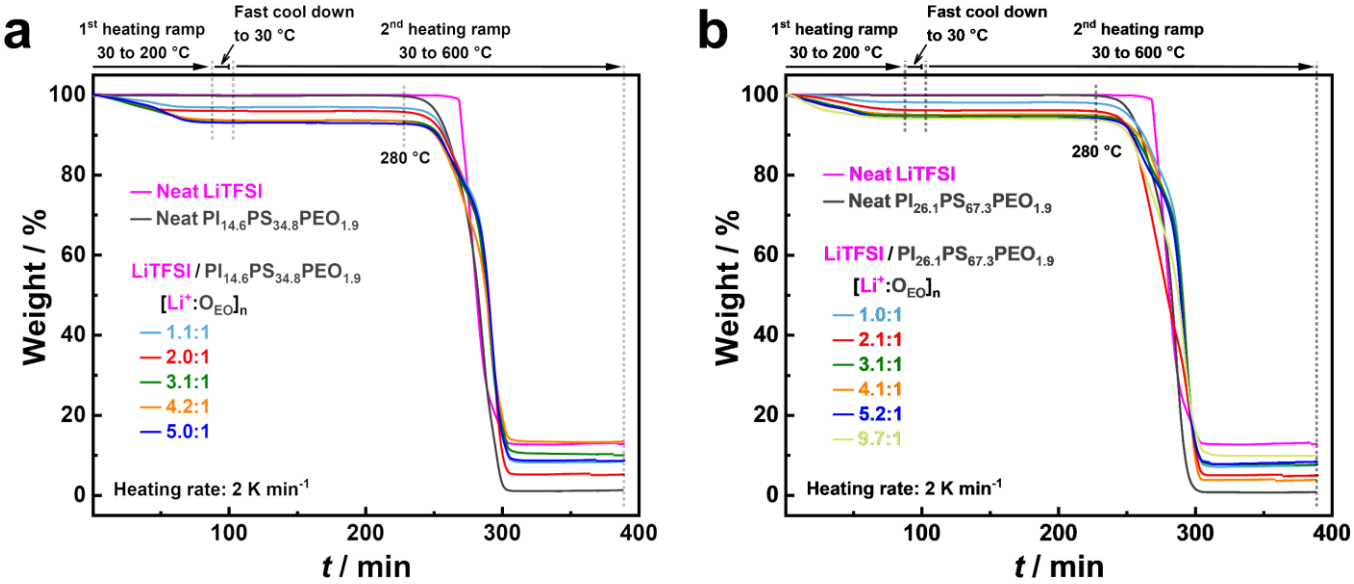

Fig. S5 | TGA curves for determination of THF content in the SPE membranes. Depicted are the TGA curve of neat $PI_xPS_yPEO_{1.9}$ BCP, neat LiTFSI, and the corresponding SPEs depending on $[Li^+:O_{EO}]_n$, respectively, with weight loss plotted against time, in **a**, for $PI_{14.6}PS_{34.8}PEO_{1.9}$, and in **b**, for $PI_{26.1}PS_{67.3}PEO_{1.9}$. A weight loss in the SPE membranes of both BCPs is seen to be proportional to the embedded LiTFSI amount. For a better overview, the weight loss was plotted against time, as the TGA measurements consist of two sequential heating ramps. The temperature profile has been simplified on the upper X-axis and the whole temperature-time profile is shown in Fig. S3. The weight loss at 280 °C is completely attributable to the evaporation of THF and was selected as the point for determining the amount of THF for all SPEs, before the decomposition of the neat BCP and LiTFSI starts at higher temperature.

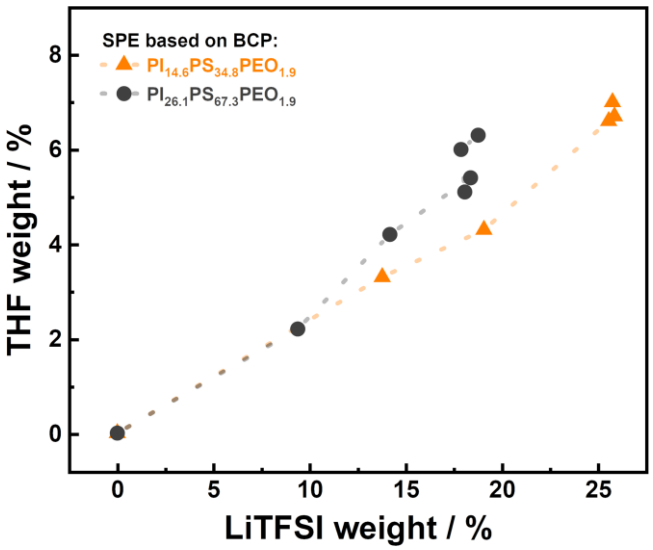

Fig. S6 | Proportional dependence between THF content and embedded LiTFSI amount. Shown is the THF content (in wt.%, determined by TGA) in dependence of the LiTFSI amount (in wt.%, determined by ^{19}F-solution-NMR) from the SPE membranes of both BCPs.

Table S1 | PI_x, PS_y and PEO block wt.% contained in neat $PI_xPS_yPEO_{1.9}$ BCPs and in the corresponding SPEs. Calculated from the $PI_xPS_yPEO_{1.9}$ wt.% existing in the SPE membrane, taking into account the embedded LiTFSI and THF quantity, and the proportion of the respective polymer block in the $PI_xPS_yPEO_{1.9}$.

$[Li^+:O_{EO}]_n$	$PI_{14.6}PS_{34.8}PEO_{1.9}$	0.0:1	1.1:1	2.0:1	3.1:1	4.2:1	5.0:1	-
	$PI_{26.1}PS_{67.3}PEO_{1.9}$	0.0:1	1.0:1	2.1:1	3.1:1	4.1:1	5.2:1	9.7:1
PI_x wt.%		28.2	23.4	21.6	19.1	19.0	19.0	-
		29.5	26.1	24.1	22.5	22.7	22.4	22.1
PS_y wt.%		68.0	56.4	52.1	46.1	45.8	45.7	-
		68.8	60.8	56.1	52.4	52.8	52.4	51.5
PEO wt.%		3.9	3.2	3.0	2.6	2.6	2.6	-
		1.7	1.5	1.4	1.3	1.3	1.3	1.3

Differential Scanning Calorimetry (DSC)

Sample preparation: Care was taken to ensure that the samples did not come into contact with air (oxygen and moisture). Therefore, all samples were prepared in a glovebox under argon atmosphere. ~10 mg of sample was placed into a Tzero®-aluminum pan, hermetically sealed, and subsequently loaded into the instrument.

Measurement set-up: The measurement was carried out with a heat flux calorimeter DSC-Q2000 (TA Instruments) with LNCS (Liquid Nitrogen Cooling System) and for precise baseline recording using

Tzero®-technology. Two heating ramps were determined in the temperature range from -140 to 190 °C with a heating rate of 10 K min^{-1} under 25 mL min^{-1} helium sample purge. The DSC signals were analyzed with the Universal Analysis 2000 software (version: 4.5A, Build 4.5.0.5., TA Instruments).

Additional information: To obtain more detailed information about the structure-giving BCP matrix and the localization of the embedded LiTFSI and THF amount in the SPE membranes, DSC measurements were performed (Fig. S7).

Neat BCPs: The neat BCPs have three characteristic thermal phase transitions, the glass transition temperature (ϑ_g) for the PI_x phase ϑ_{g,PI_x} around -67 °C, the ϑ_{g,PS_y} for the PS_y phase in the range of 87 to 96 °C, as well as the melting point (ϑ_{mp}) $\vartheta_{mp,PEO}$ of the PEO at 50 °C, whereby the latter is not detectable for $PI_{26.1}PS_{67.3}PEO_{1.9}$.[21]

SPE membranes: It is directly evident from Fig. S7, that no $\vartheta_{mp,PEO}$ is observed for all SPEs, indicating that the PEO phase is no longer crystalline. The simultaneous occurrence of the ϑ_{g,PI_x} and ϑ_{g,PS_y} leads to the conclusion that the structuring polymer matrix is microphase-separated in all SPEs. Due to the microphase separation, the PI_x and PS_y block behave independently from each other such as if they were a neat, single polymer block. Consequently, their heat capacity change (ΔC_p) is proportional to the respective block weight fraction in the SPE (Table S1). As can be seen in Table S2, the $\Delta C_{p,PS_y}$ values decrease with increasing LiTFSI and THF quantity in the SPEs of both BCPs and remain constant when the LiTFSI saturation limit is reached, thus behaving inversely proportional to the determined LiTFSI and THF content, which can be attributed to the reduction of the BCP weight fraction in the SPE.

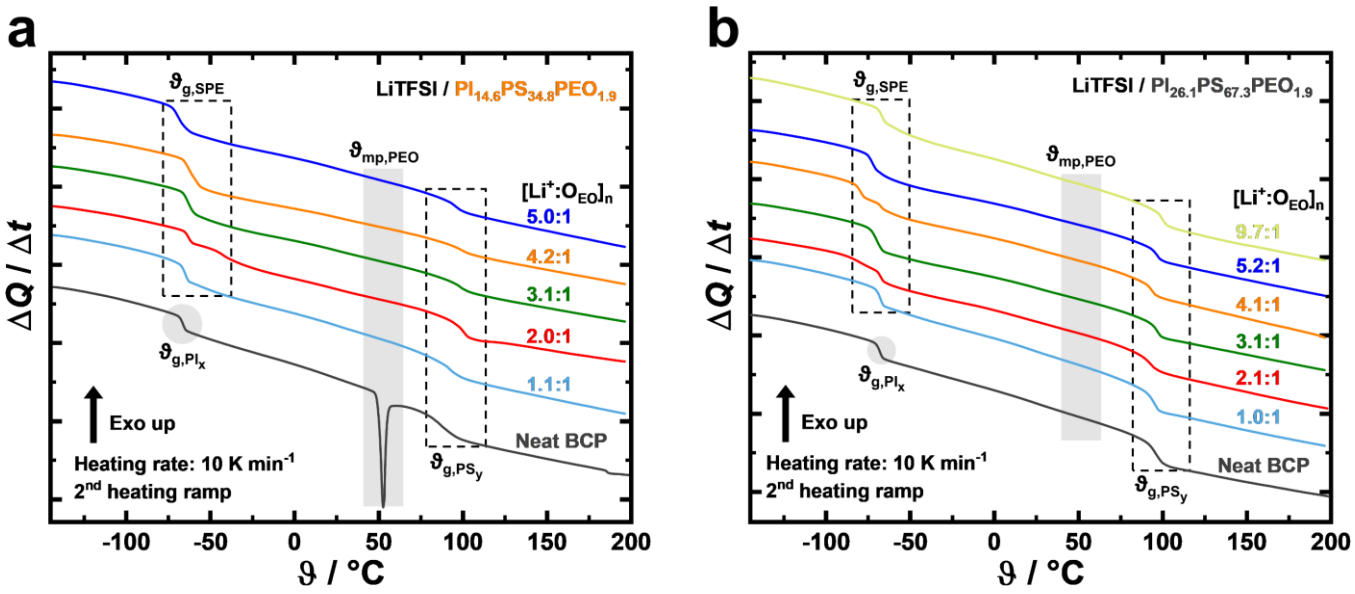

Fig. S7 | DSC measurements of SPE membranes depending on $[Li^+:O_{EO}]_n$ and the respective neat BCPs, in **a**, for $PI_{14.6}PS_{34.8}PEO_{1.9}$, and in **b**, for $PI_{26.1}PS_{67.3}PEO_{1.9}$. The simultaneous occurrence of the ϑ_g for the PI_x and PS_y blocks of the structuring BCP matrix indicates that both are microphase-separated in all SPEs. The absence of $\vartheta_{mp,PEO}$ due to the embedding of LiTFSI and THF together with the appearance of $\vartheta_{g,SPE}$ in the temperature range of -70 to -60 °C (Fig. 1b) indicate that LiTFSI, PEO and THF form a common ternary phase that is microphase-separated from the PI_x and PS_y polymer blocks in the SPEs.

A ϑ_g in the range of -70 to -60 °C can be seen for all SPEs (Fig. S7), which is consistent with the expected ϑ_{g,PI_x} from temperature, but differs in shape and width depending on $[Li^+:O_{EO}]_n$, in some cases also consisting of at least two overlapping ϑ_g signals. Especially compared to the neat BCPs, a clear difference can be observed. Notably, the ΔC_p of the ϑ_g signals in this temperature range increases proportionally to the determined quantity of LiTFSI and THF for all SPEs of both BCPs (Table S2) and is notably than the $\Delta C_{p,PI_x}$ of the corresponding neat BCP, although the weight fraction of the PI_x block in the SPEs decreases (Table S1). Consequently, in the SPEs, this ϑ_g is composed of other overlapping signals in addition to the ϑ_{g,PI_x} signal. As there is only the embedded LiTFSI and THF amount in the SPEs besides the structuring BCP matrix and the $\vartheta_{mp,PEO}$ disappears, it is likely that the observed signal overlap comes from LiTFSI/PEO, LiTFSI/THF or LiTFSI/PEO/THF mixtures, so these mixtures were investigated in more detail.

Table S2 | Results of thermal analysis by DSC measurements of all SPEs from both BCPs.

$[Li^+:O_{EO}]_n$	$PI_{14.6}PS_{34.8}PEO_{1.9}$	0.0:1	1.1:1	2.0:1	3.1:1	4.2:1	5.0:1	-
	$PI_{26.1}PS_{67.3}PEO_{1.9}$	0.0:1	1.0:1	2.1:1	3.1:1	4.1:1	5.2:1	9.7:1
$\vartheta_{g,SPE}$ [a] / °C		-65.9 [b]	-64.8	-60.6	-62.5	-61.2	-68.0	-
		-67.6 [b]	-67.5	-68.2	-69.6	-77.8	-71.2	-65.7
$\Delta C_{p,SPE}$ [a] / J (g K)$^{-1}$		0.141 [b]	0.175	0.190	0.204	0.210	0.208	-
		0.136 [b]	0.164	0.176	0.190	0.187	0.189	0.191
ϑ_{g,PS_y} / °C		86.8	92.8	99.2	98.8	98.0	96.6	-
		95.8	94.4	92.3	96.2	93.0	96.1	99.9
$\Delta C_{p,PS_y}$ / J (g K)$^{-1}$		0.237	0.195	0.184	0.159	0.162	0.161	-
		0.205	0.184	0.168	0.157	0.152	0.154	0.155

[a] Consists of ϑ_{g,PI_x}, $\vartheta_{g,LiTFSI/PEO}$, $\vartheta_{g,LiTFSI/THF}$ and $\vartheta_{g,LiTFSI/PEO/THF}$ signals. [b] Values only for the PI_x block from the neat BCPs.

Effect of LiTFSI content on $\vartheta_{mp,PEO}$: As seen in Fig. S8, for the neat PEO block of the BCPs, a $\vartheta_{mp,PEO}$ at 50 °C is observed, but no additional ϑ_g appears, consequently it is crystalline. Due to embedding of LiTFSI into the PEO phase, the crystalline structure of PEO is disturbed, and thus the LiTFSI/PEO mixture becomes amorphous, resulting in the appearance of a $\vartheta_{g,LiTFSI/PEO}$. For the mixture with the lowest $[Li^+:O_{EO}]$ of 0.07:1, in addition to the $\vartheta_{g,LiTFSI/PEO}$ at ~-45 °C, a melt crystallization of PEO occurs. This implies that an exothermic crystallization signal occurs first, followed by an endothermic $\vartheta_{mp,PEO}$. Whereby the melting enthalpy is substantially weaker and shifted to lower temperature compared to neat PEO as only a semi-crystalline structure can be formed due to the embedded LiTFSI amount. In both mixtures with the higher $[Li^+:O_{EO}]$ of 0.10:1 and 0.14:1, only the $\vartheta_{g,LiTFSI/PEO}$ can be detected in the range of -40 to -30 °C, which is shifted to higher temperature with increasing LiTFSI content.[58] The $\vartheta_{mp,PEO}$ has disappeared as sufficient LiTFSI is within the PEO, making it completely amorphous. Therefore, due to the embedding of the LiTFSI, this behavior and the $\vartheta_{g,LiTFSI/PEO}$ of the amorphous mixture is also observed in the PEO phase of the SPEs.

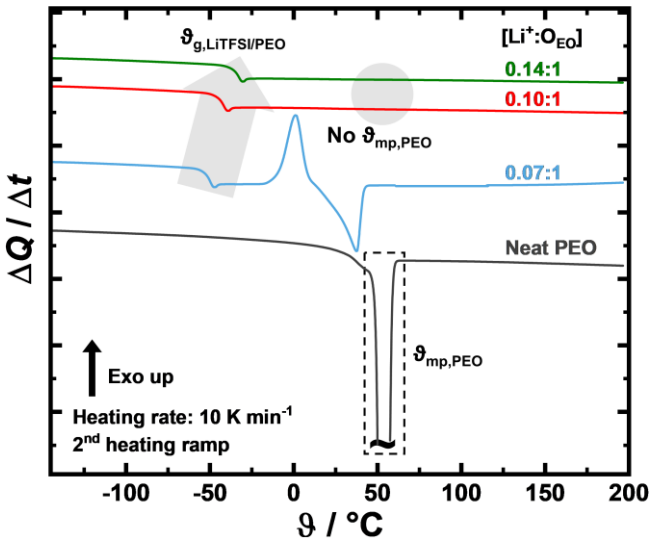

Fig. S8 | Effect of LiTFSI content on $\vartheta_{mp,PEO}$. DSC measurements of neat PEO and mixtures of LiTFSI/PEO depending on the [Li^+:O_{EO}]. For the neat PEO, a $\vartheta_{mp,PEO}$ at 50 °C is observed. Embedding of LiTFSI into PEO leads to disturbance of the crystalline PEO structure, the resulting mixture becomes amorphous, and a $\vartheta_{g,LiTFSI/PEO}$ is obtained. With sufficient LiTFSI within the PEO, the mixture is completely amorphous and no $\vartheta_{mp,PEO}$ occurs.

Effect of LiTFSI content on $\vartheta_{g,LiTFSI/THF}$: Fig. S9a shows DSC measurements of different binary LiTFSI/THF mixtures depending on the [Li^+:O_{THF}]. As seen in Fig. S9b, increasing the LiTFSI content from [Li^+:O_{THF}] = 0.33:1 to 1.02:1 leads to an exponential temperature rise of the $\vartheta_{g,LiTFSI/THF}$ from -106.1 to -52.4 °C.[59] The corresponding $\Delta C_{p,LiTFSI/THF}$, listed in Table S3, are roughly the same for all mixtures, averaging ~0.34 J $(g\ K)^{-1}$ with a slight reduction with increasing Li^+ content. The $\vartheta_{g,LiTFSI/THF}$ are consistent with the ϑ_g signal overlap in the SPEs in the temperature range of -70 to -60 °C, for those mixture compositions that are most closely matching the determined amount of LiTFSI and THF in the SPEs.

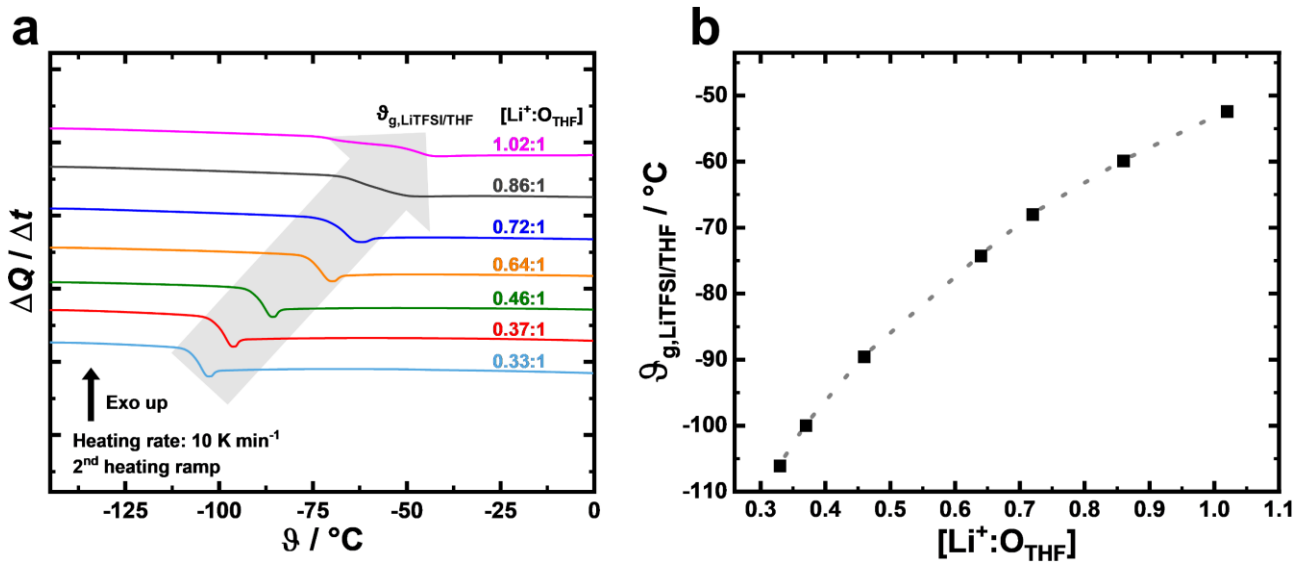

Fig. S9 | Effect of LiTFSI content on $\vartheta_{g,LiTFSI/THF}$. a, DSC measurements of LiTFSI/THF mixtures depending on the [Li^+:O_{THF}]. As a result, an increase of the Li^+ content, leads to a shift of the $\vartheta_{g,LiTFSI/THF}$ to higher temperature. If the compositions of the LiTFSI/THF mixtures correspond to the determined LiTFSI and THF content in the SPEs, the ϑ_g are in the same temperature range. **b**, Plot of the determined $\vartheta_{g,LiTFSI/THF}$ in dependence of the [Li^+:O_{THF}], which increases exponentially with rising LiTFSI amount.[59]

Table S3 | Thermal analysis results obtained by DSC measurements of different binary LiTFSI/THF mixtures.

[Li^+:O_{THF}]	$\vartheta_{g,LiTFSI/THF}$ / °C	$\Delta C_{p,LiTFSI/THF}$ / J (g K)$^{-1}$
0.33:1	-106.1	0.363
0.37:1	-100.0	0.357
0.46:1	-89.6	0.346
0.64:1	-74.3	0.331
0.72:1	-68.0	0.326
0.86:1	-59.9	0.320
1.02:1	-52.4	0.315

Effect of LiTFSI content on $\vartheta_{g,LiTFSI/PEO/THF}$: DSC measurements of LiTFSI/PEO/THF mixtures depending on the [Li^+:O_{EO+THF}] are shown in Fig. S10. The [Li^+:O_{EO+THF}] refers to the ratio between Li^+ and the O-donor atoms from THF and PEO, whereby for the PEO, the O-atoms are calculated from the substance mass and the number of monomer units. The composition of each component in the LiTFSI/PEO/THF mixtures is related to each other in a ratio that is similar to the expected average from the quantifications of the SPEs (Table S4). As a result, an increase of LiTFSI content leads to a shift of the $\vartheta_{g,LiTFSI/PEO/THF}$ to higher temperature, and all three mixtures are in the temperature range of -50 to -70 °C and thus in the ϑ_g signal overlap range observed for SPEs. The $\Delta C_{p,LiTFSI/PEO/THF}$ for all three mixtures is 0.34 J (g K)$^{-1}$ (Table S4), which is approximately the same as that for the binary LiTFSI/THF mixtures.

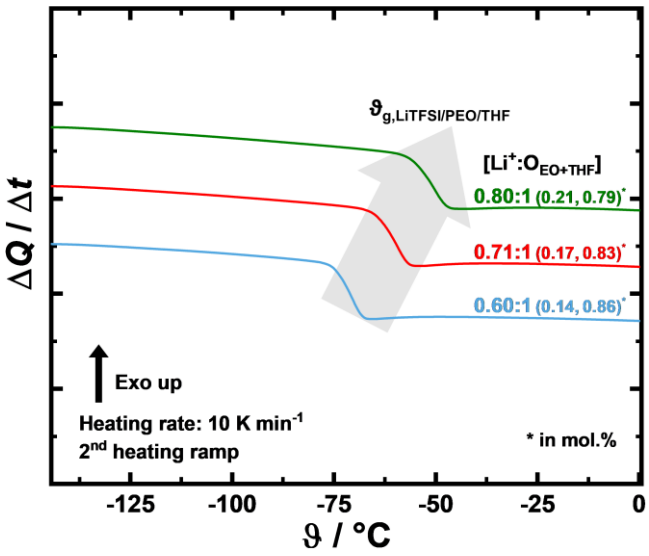

Fig. S10 | Effect of LiTFSI content on $\vartheta_{g,LiTFSI/PEO/THF}$. DSC measurements of LiTFSI/PEO/THF mixtures depending on the [Li^+:O_{EO+THF}]. The [Li^+:O_{EO+THF}] refers to the ratio between Li^+ and the O-donor atoms from THF and PEO, whereby for the PEO, the O-atoms are calculated from the substance mass and the number of monomer units. The molar ratio of the O-atoms from the PEO and THF to each other is shown in the brackets in mol.%. The individual component ratios were chosen to match the determined composition of the SPEs (Table S4) and all three mixtures are in the temperature range of -50 to -70 °C and thus in the ϑ_g signal overlap range observed for SPEs.

Table S4 | Sample weights and DSC results of the ternary LiTFSI/PEO/THF mixtures.

[Li^+:O_{EO+THF} a)]	[Li^+] / mmol	[O_{EO}] b) / mmol	[O_{THF}] / mmol	$\vartheta_{g,SPE}$ c) / °C	$\Delta C_{p,SPE}$ c) / J (g K)$^{-1}$
0.60:1 (0.14, 0.86)	2.39	5.57 10^{-1}	3.43	-71.3	0.343
0.71:1 (0.17, 0.83)	2.38	5.84 10^{-1}	2.78	-60.6	0.345
0.80:1 (0.21, 0.79)	2.41	6.16 10^{-1}	2.38	-51.4	0.340

a) In mol.%. b) Calculated from the sample weight and the number of monomer units in PEO. c) Ternary LiTFSI/PEO/THF mixtures.

Contributions to the $\vartheta_{g,SPE}$: Using the ΔC_p, the characteristic signals overlapping in the temperature range from -70 to -60 °C in the SPEs and contributing to the $\vartheta_{g,SPE}$ can be assigned to the PI_x block, the binary LiTFSI/PEO and LiTFSI/THF mixtures, and the ternary LiTFSI/PEO/THF mixtures. Thus, the $\Delta C_{p,SPE}$ can be calculated from the sum of the respective individual signals considering their respective ΔC_p value and the determined weight proportion in the SPE by using Eq. (S1) and is similar to the determined $\Delta C_{p,SPE}$ values of the SPEs from Table S2. Therefore, the DSC results are consistent with the LiTFSI and THF quantification results.

$$\Delta C_{p,SPE} = \Delta C_{p,PI_x}\, w_{PI_x} + \Delta C_{p,LiTFSI/PEO/THF}\,(w_{LiTFSI} + w_{PEO} + w_{THF}) \qquad (S1)$$

In Eq. (S1), w_i represents the mass fraction in wt.% of LiTFSI (Table 1), PEO (Table S1) and THF (Table 1) in the SPEs. As previously described, it is assumed that

$\Delta C_{p,LiTFSI/THF} = \Delta C_{p,LiTFSI/PEO/THF} = 0.34$ J (g K)$^{-1}$ (Table S3, Table S4) and $\Delta C_{p,PI_x} = 0.14$ J (g K)$^{-1}$ (Table S2). Due to the fact that $\Delta C_{p,PI_x}$ in the neat BCPs is much smaller than $\Delta C_{p,LiTFSI/THF}$ and $\Delta C_{p,LiTFSI/PEO/THF}$, $\Delta C_{p,SPE}$ increases proportionally to the embedded LiTFSI and THF amounts.

Effect of LiTFSI content on $\vartheta_{mp,THF}$: In Fig. S11, DSC measurements of neat THF and of binary LiTFSI/THF mixtures depending on [Li^+:O_{THF}] are shown. The melting point of neat and uncoordinated THF ($\vartheta_{mp,THF}$) is -105 °C, whose melting point enthalpy is reduced with increasing LiTFSI content until no $\vartheta_{mp,THF}$ can be detected at [Li^+:O_{THF}] ≥0.25:1. Consequently, with increasing LiTFSI content, the THF molecules are coordinated to the Li^+ until at [Li^+:O_{THF}] ≥0.25:1 all of them are coordinated, the $\vartheta_{mp,THF}$ disappears, and the Li^+ is tetrahedrally surrounded by THF. In the SPEs, no $\vartheta_{mp,THF}$ is seen (Fig. S7), clearly indicating that all THF is coordinated to LiTFSI and therefore, during controlled solution casting, all THF is selectively embedded only in the PEO phase in addition to the total LiTFSI quantity.

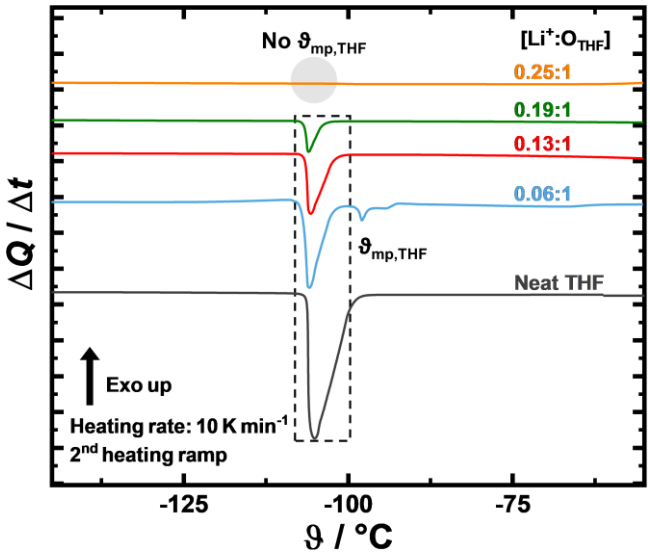

Fig. S11 | Effect of LiTFSI content on $\vartheta_{mp,THF}$. DSC measurements of neat THF and LiTFSI/THF mixtures depending on the [Li^+:O_{THF}]. $\vartheta_{mp,THF}$ of neat and uncoordinated THF is -105 °C, and its melting point enthalpy is reduced with increasing LiTFSI content until at [Li^+:O_{THF}] ≥0.25:1 no $\vartheta_{mp,THF}$ can be detected. Consequently, there is no uncoordinated THF, as all O-atoms tetrahedrally coordinate the Li^+.

X-Ray Diffraction (XRD) respectively Wide-Angle X-Ray Scattering (WAXS)

Sample preparation: For WAXS measurement, the neat BCP and the SPE membranes were carefully broken into smaller pieces in order to get the sample into the glass capillary (borosilicate glass, outer diameter = 2.1 mm, wall thickness = 0.05 mm) in a dryroom. The filled glass capillary was sealed tightly.

Measurement set-up: WAXS measurements were performed using the laboratory-based "Ganesha-Air" system (SAXSLAB/XENOCS) equipped with a D2-MetalJet (Excillum) anode operating at 70 kV and 3.57 mA with Ga-Kα radiation (wavelength λ = 0.134 nm). The beam is focused with a focal length of 55 cm to provide a 100 µm intense beam at the sample position. Two pairs of scatterless slits are used to adjust the beam size depending on the detector distance. WAXS data with a position-sensitive PILATUS 100k detector (Detris). The detector distances were calibrated with silicon.

Additional information: The reflex positions for the triclinic unit cell with dimensions a = 0.47 nm, b = 1.29 nm, c = 1.53 nm and angles $\alpha = 82.5°$, $\beta = \gamma = 89°$ were calculated from the Eq. (S2)

$$q = 2\pi(1-(\cos\alpha)^2-(\cos\beta)^2-(\cos\gamma)^2+2\cos\alpha\cos\beta\cos\gamma)^{-1}\left(\frac{h^2}{a^2}(\sin\alpha)^2+\frac{k^2}{b^2}(\sin\beta)^2+\frac{l^2}{c^2}(\sin\gamma)^2\right.$$
$$\left.+\frac{2kl}{bc}(\cos\beta\cos\gamma-\cos\alpha)+\frac{2lh}{ca}(\cos\gamma\cos\alpha-\cos\beta)+\frac{2hk}{ba}(\cos\alpha\cos\beta-\cos\gamma)\right) \quad \text{(S2)}$$

and are indicated in Fig. 2a.

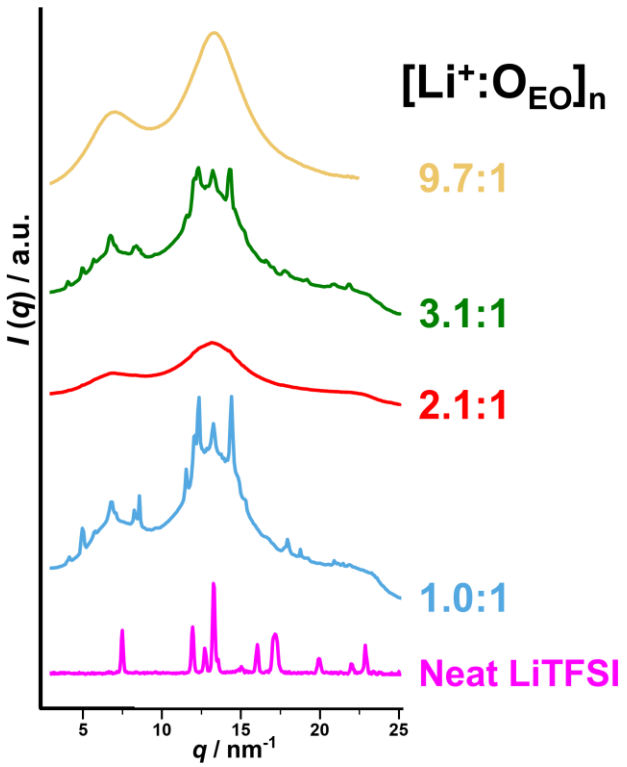

Fig. S12 | WAXS measurements at room temperature of neat LiTFSI and SPEs of LiTFSI/$PI_{26.1}PS_{67.3}PEO_{1.9}$ depending on $[Li^+:O_{EO}]_n$ based.

Solid-State $^{19}F\{^{1}H\}$ Heteronuclear Overhauser Effect Spectroscopy (HOESY)-NMR

Sample preparation: The SPE membrane was packed in a 4 mm ZrO_2 thin wall rotor with a Vespel cap in a dry room to exclude moisture.

Measurement set-up: 2D solid-state $^{19}F\{^{1}H\}$ heteronuclear Overhauser effect spectroscopy (HOESY-NMR) [54] measurements were performed to localize and analyze the environment of the LiTFSI in the SPE membranes. Spectra were recorded on a Bruker Avance Neo spectrometer operating at the static field of 11.76 T of a Bruker Ascend wide-bore magnet ($\nu_L(^{1}H)$ = 500.39 MHz; $\nu_L(^{19}F)$ = 470.80 MHz). A commercial Bruker 4 mm H/F/X DVT MAS probe equipped with magic angle gradient coils was used to acquire the spectra. The magic angle was calibrated prior to the measurements by optimizing the spinning-sideband intensity in the ^{23}Na spectrum of solid $NaNO_3$ spinning at 5 kHz. The chemical shifts of ^{1}H and ^{19}F were externally referenced against solid adamantane ($\delta(^{1}H)$ = 1.85 ppm) [55] and PTFE tape ($\delta(^{19}F)$ = −122.0 ppm) [56] before the measurement using the replacement method. These samples were also used to calibrate the r.f. pulse lengths. The ^{1}H and ^{19}F pulses were fed to the H/F channel of the probe using a frequency diplexer along with two bandpass filters on each channel to separate the ^{19}F signal from all ^{1}H frequencies during acquisition. 90° pulse lengths of 5 μs were applied for both nuclei. The sample was spinning at 5 kHz using dry N_2 as driving gas at ambient temperature. A ^{19}F relaxation delay of 1 s was chosen after an initial saturation comb between each of the 64 scans acquired for each indirect dimension increment. 196 indirect increments were acquired with a 200 μs (rotor synchronous) increment in the indirect evolution time. Frequency discrimination in the indirect ^{1}H dimension was achieved using the States-TPPI scheme. The NOE mixing time was also chosen to 1 s.

Additional information: The spatial relationships between protons (^{1}H) from the THF and the ^{19}F heteronucleus from the LiTFSI can be investigated when they are spatially very close to each other to allow for cross-relaxation *via* the heteronuclear Overhauser effect. Both spectra show a correlation of the $TFSI^-$ ^{19}F signal at -79.47 ppm to the signals of the THF α- and β-protons at 3.67 ppm and 1.77 ppm, respectively. The overall conclusion is that all $TFSI^-$ species coordinate to the THF. As the chemical shift of the PEO protons and the THF α-protons are indistinguishable here, it is not possible to differentiate between correlation to PEO and THF using only the signal at 3.67 ppm. However, since both correlation signals have the same intensity, it can be concluded that also the correlation at 3.67 ppm arises mainly due to a NOE between $TFSI^-$ and THF.

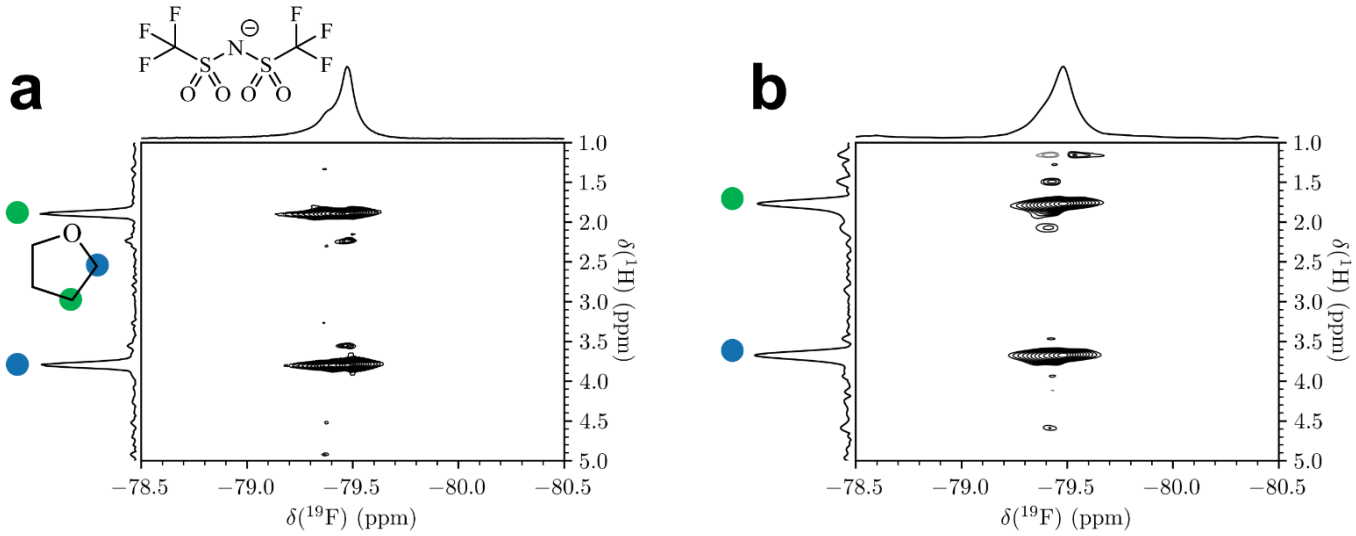

Fig. S13 | 2D-solid-state $^{19}F\{^{1}H\}$ HOESY MAS NMR spectrum of THF and TFSI$^-$ from a SPE membrane consisting of $PI_{14.6}PS_{34.8}PEO_{1.9}$ with $[Li^+:O_{EO}]_n$ = 4.2:1 spinning at 5 kHz (HOESY = heteronuclear Overhauser effect spectroscopy). In **a**, before and in **b**, after annealing. A NOE mixing time of 1 s was chosen in both experiments. In both spectra, only a correlation of the TFSI$^-$ anion to the THF protons is observed.

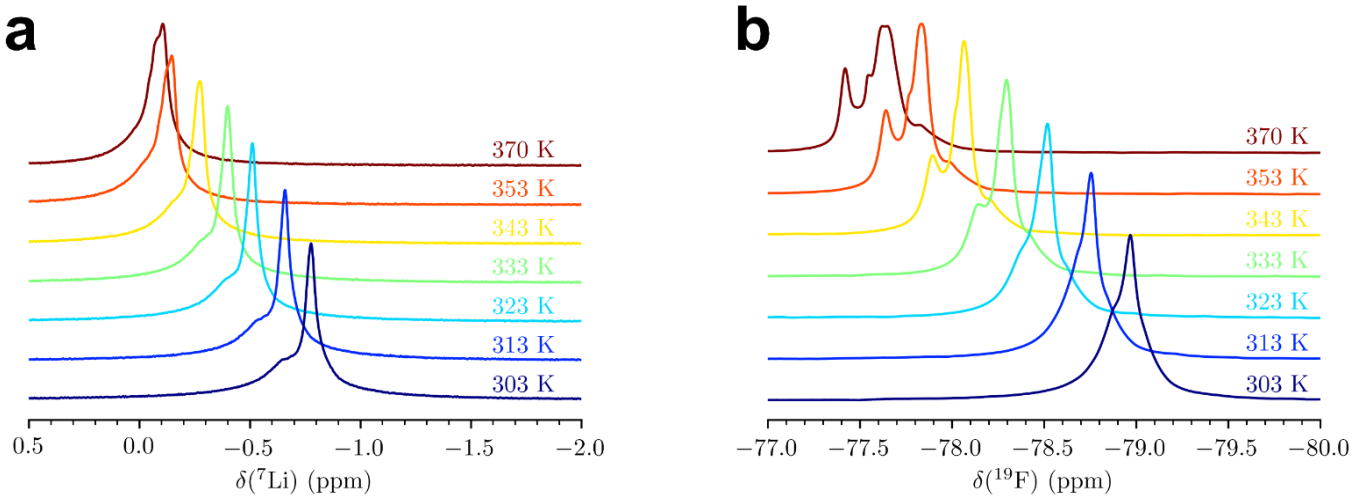

Fig. S14 | Temperature-dependent solid-state MAS NMR measurements LiTFSI from a SPE membrane consisting of $PI_{14.6}PS_{34.8}PEO_{1.9}$ with $[Li^+:O_{EO}]_n$ = 4.2:1. The temperature ranges from 90 to 30 °C, during cooling. In **a**, for ^{7}Li and in **b**, for ^{19}F. Several defined environments of Li^+ and TFSI$^-$ showing clear temperature dependence.

Calculation of PEO Volume Fraction

The ϕ_{PEO} of the common LiTFSI/PEO/THF phase forming in the SPEs was calculated from the individual masses and published densities (ρ_{THF} = 0.89,[28] ρ_{LiTFSI} = 2.25 [29] in g cm^{-3}).

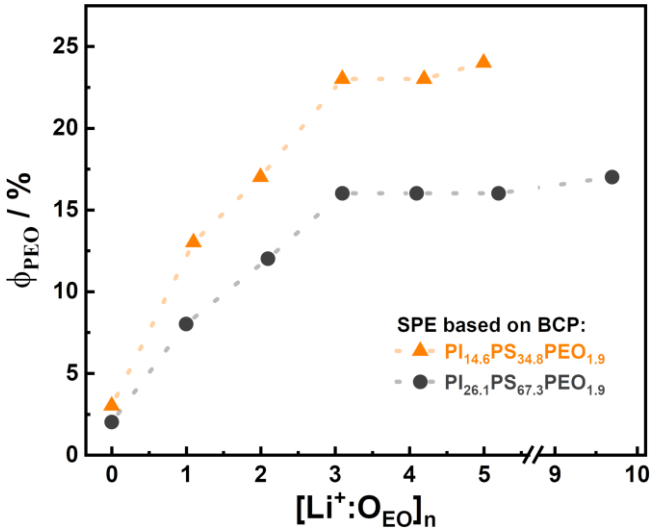

Fig. S15 | Swelling of the PEO phase in SPEs. Volume fraction of the PEO phase (ϕ_{PEO}) in dependence of $[Li^+:O_{EO}]_n$ in the SPEs from both BCPs, where, in addition to the PEO, the volume of the embedded THF and LiTFSI has to be taken into account.

Electron Microscopy

Sample preparation and cryo-ultramicrotomy: The SPE samples were embedded inside a glove box in EPOTEK resin to prevent them from humidity during transport. The embedded sample was roughly pre-trimmed by a Leica EM Trim to remove most of the resin, but still keep the sample completely covered. The sample then was transferred to a Leica UC7 ultramicrotome with attached cryo chamber FC7 and pre-cooled by liquid nitrogen to -80 to -100 °C depending on the sample. The sample then was further trimmed using a glass knife to remove the remaining resin. Subsequently a diamond trimming knife from Diatome was used to trim the final block face. Sectioning was performed with a cryo diamond knife (Diatome, 35°, for dry sectioning) using the following temperature settings: knife: sample: chamber: Cutting thickness was set in the range of 80 - 100 nm. Samples were transferred to carbon coated cupper grids of 200 mesh. Samples containing LiTFSI were stored in liquid nitrogen.

Care was taken to handle all samples under exclusion of air and moisture. During sectioning and when transferred to the grid, the samples were always covered by a nitrogen atmosphere blanket inside the cryo chamber of the ultramicrotome. The sections were stored in liquid nitrogen and transferred to a TEM using a cryo transfer holder.

Measurement set-up: SEM measurements on plain BCP samples were performed at room temperature using a Thermo Fisher volumescope using a STEM detector in bright field mode at 30 kV. The low acceleration voltage of the SEM enables high contrast imaging without staining.

TEM measurements were done using a JEOL F200 (Cryo)-transmission electron microscope operated at 200 kV in STEM mode. A Fischione cryo transfer holder 2550 was used to cool the samples to -177 °C to minimize beam damage. Within the cooled station of the cryo transfer holder the samples could be kept under nitrogen atmosphere during insertion into the holder. During transfer of the holder into the microscope, the grid is inserted into the tip of the holder to prevent contact to air and humidity. Mostly no ice contamination is found on the sections.

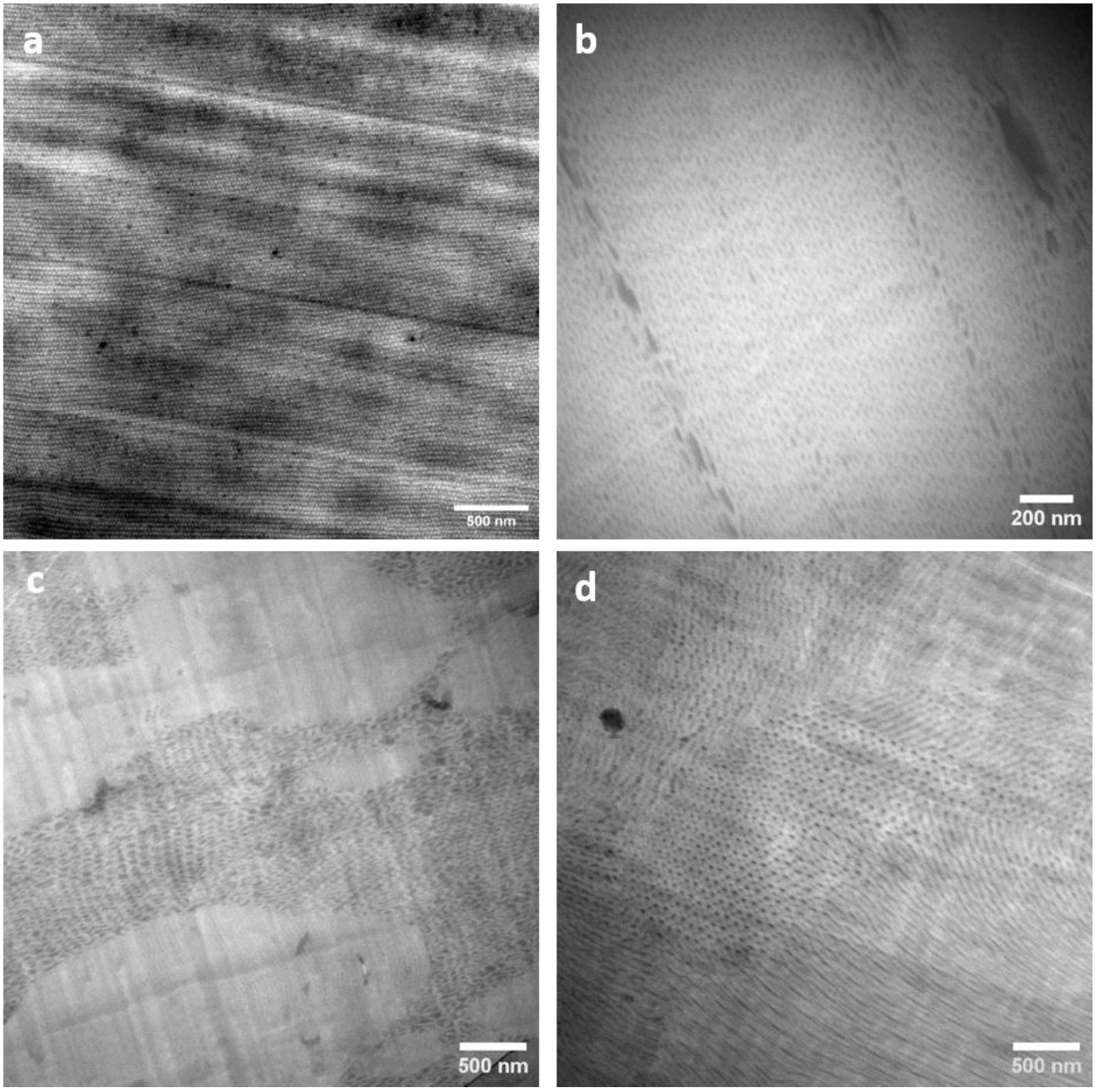

Fig. S16 | STEM overview images of SPEs from $PI_xPS_yPEO_{1.9}$ block copolymer morphologies with increasing LiTFSI concentrations. **a**, Hexagonally ordered cylindrical morphology (HEX) of the neat $PI_{14.6}PS_{34.8}PEO_{1.9}$ block copolymer. **b**, Ordered Fddd network structure observed for the SPEs from the same block copolymer at $[Li^+:O_{EO}]_n$ = 1.1:1, exhibiting alternating domains characteristic for the (110) projection. **c**, Gyroid structure observed for the SPE from the same block copolymer at $[Li^+:O_{EO}]_n$ = 4.2:1 with the undulating domain pattern characteristic for the (211) projection. **d**, Fddd network structure observed for the SPE from the $PI_{26.1}PS_{67.3}PEO_{1.9}$ block copolymer at a LiTFSI concentration of $[Li^+:O_{EO}]_n$ = 9.7:1 corresponding to the (001) projection.

Small-Angle X-Ray Scattering (SAXS)

Sample preparation: For SAXS measurement, the neat BCP and the SPE membranes were carefully broken into smaller pieces in order to get the sample into the glass capillary (borosilicate glass, outer diameter = 2.1 mm, wall thickness = 0.05 mm) in a dryroom. The filled glass capillary was sealed tightly.

Measurement set-up: SAXS measurements were performed using the laboratory-based "Ganesha-Air" system (SAXSLAB/XENOCS) equipped with a D2-MetalJet (Excillum) anode operating at 70 kV and 3.57 mA with Ga-Kα radiation (wavelength λ = 0.134 nm). The beam is focused with a focal length of 55 cm to provide a 100 μm intense beam at the sample position. Two pairs of scatterless slits are used to adjust the beam size depending on the detector distance. SAXS data with a position-sensitive PILATUS 300k detector (Detris). After calibration with silver behenate, the distance from the sample to the detector was set to 950 and 350 mm resulting in a *Q*-range 0.13 - 6.00 nm^{-1}. Data reduction and background subtraction was done using the Python-based project Jscatter [57].

Additional information: For the annealing experiment the SPE membrane was annealed at 90 °C for 17 hours and one measurement was recorded every hour. The model scatterings curves for the Fddd and gyroid structure were performed using the *q*-values and multiplicities of the allowed reflections of the respective space groups (Fddd, Ia3d), assuming Gaussian peak shapes.

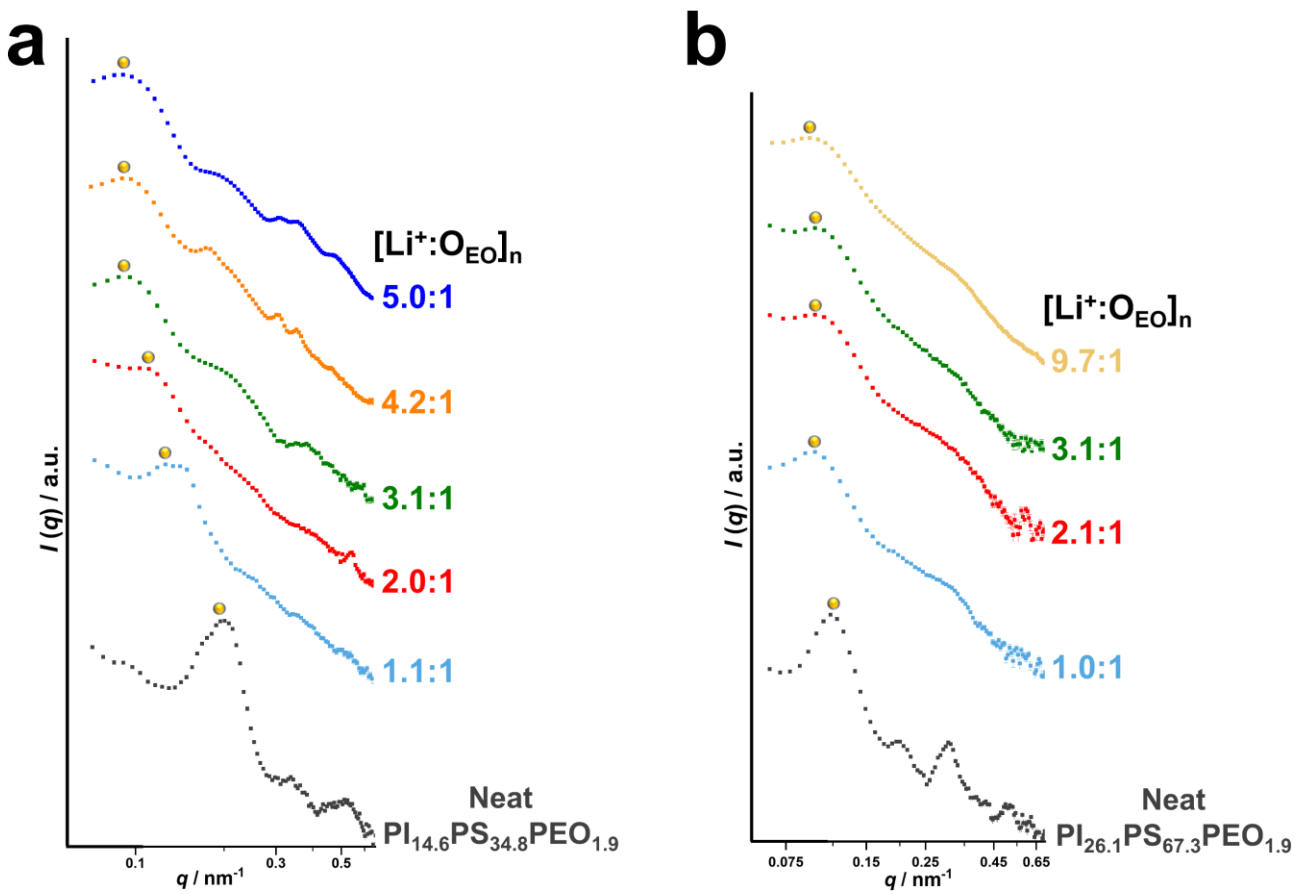

Fig. S17 | SAXS measurements of SPE membranes. Room temperature SAXS measurements depending on $[Li^+:O_{EO}]_n$ in **a**, of neat $PI_{14.6}PS_{34.8}PEO_{1.9}$ and the corresponding SPEs and in **b**, of neat $PI_{26.1}PS_{67.3}PEO_{1.9}$ and the corresponding SPEs. The first determined reflection peak (q^*) is marked by a yellow filled circle.

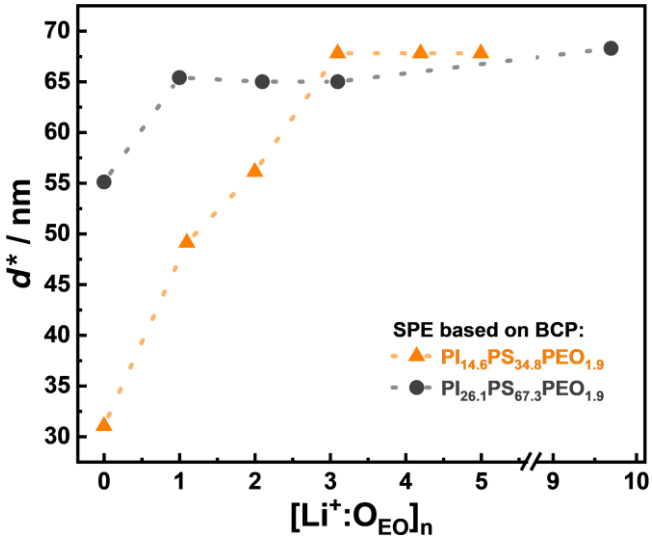

Fig. S18 | Enlargement of the average long period (*d)** depending on $[Li^+:O_{EO}]_n$ of SPEs from both BCPs, where d^* corresponds to the unit cell size, calculated according to: $d^* = 2\pi\,(q^*)^{-1}$, taking the position of the first scattering peak (q^*) directly from the SAXS measurement (Fig. S17). d^* increases proportionally with the determined amount of LiTFSI and THF, and reaches a plateau value for $[Li^+:O_{EO}]_n \geq 3.1{:}1$, which is consistent with the plateau value observed in the ^{19}F-NMR quantification experiments (Fig. 1a).

In order to track a possible structural transformation process indicated by EIS measurements on SPE membranes during annealing up to 90 °C and long-term storage at room temperature due to the considerable increase of the σ, a series of SAXS measurements were performed on a SPE membrane at 90 °C, with one measurement recorded every hour, for a total period of 17 hours. The LiTFSI/$PI_{14.6}PS_{34.8}PEO_{1.9}$/THF with $[Li^+:O_{EO}]_n$ = 5.0:1 SPE membrane was annealed at 90 °C, because at this temperature is approximately the ϑ_{g,PS_y}. Since the ϑ_{g,PI_x} is already at ~-70 °C, thus the mobility of both structuring BCP matrix blocks is increased, allowing a faster structural transformation process. As can be seen in the corresponding SAXS results from Fig. S19a, *q** remains constant during annealing, but the signals at higher *q*-values change with increasing annealing time as more and clearer signals appear. This change in the SAXS curves can be attributed to the structural features due to the transformation of the Fddd to a Gyr network phase, as shown in Fig. S19b. Therefore, the superior Gyr structure forms during annealing, which is optimal for the Li^+ transport. Moreover, in addition, the domain size can be increased (as indicated by more distinct signals), further favoring Li^+ transport.

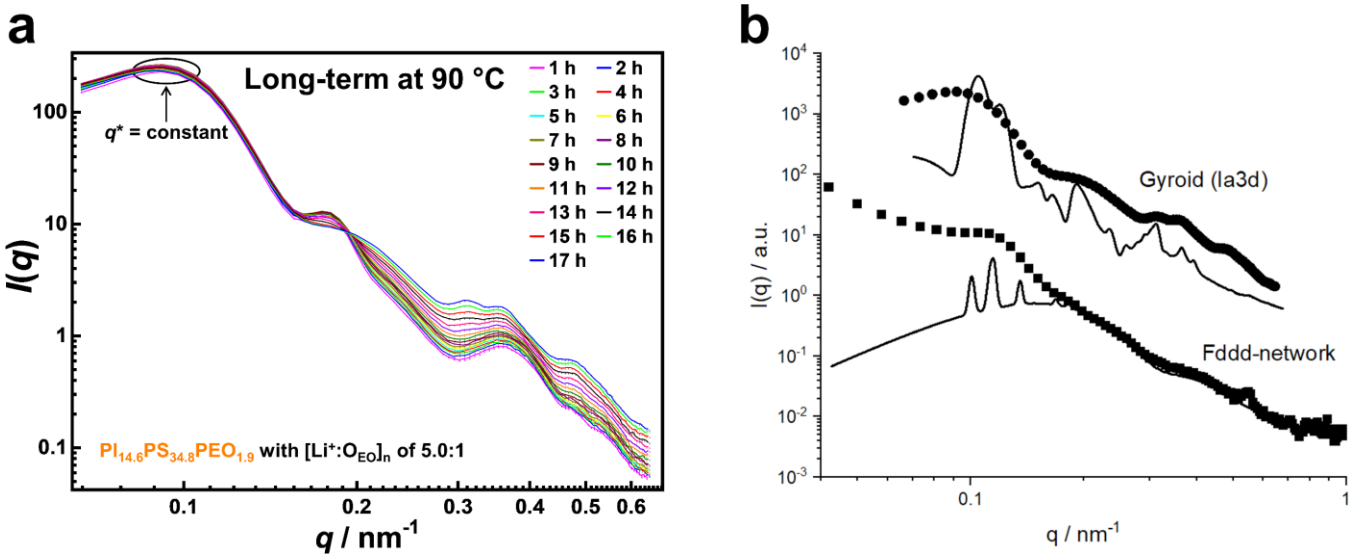

Fig. S19 | Long-term SAXS measurement to track the annealing process of a SPE membrane at 90 °C. The SPE consists of LiTFSI/$PI_{14.6}PS_{34.8}PEO_{1.9}$/THF with $[Li^+:O_{EO}]_n$ = 5.0:1. **a**, Course of the SAXS curves during annealing for 17 h at 90 °C. The signals change at higher *q*-values during the annealing time, as more and clearer signals appear. **b**, Modelling of the SAXS curves at the beginning (Fddd) and at the end (Gyroid) of the annealing procedure.

Electrochemical Impedance Spectroscopy (EIS)

Sample preparation: After the casting process, the resulting SPE membrane was pressed in a dry room to the desired membrane thickness (250 -500 µm), a circular piece was punched out (diameter = 6 - 10 mm) and used for EIS measurements.

Measurement set-up: The measurements were performed using a multi potentiostat M204 with FRA32 module and the software Nova 2.1.4 (Metrohm Autolab B.V.) in a logarithmic frequency range from 1 Hz to 1 MHz and an alternating amplitude of 40 mV. The temperature was controlled using a climatic oven (Binder MK 53). The σ was determined by placing the prepared SPE membranes in contact between two ion-blocking stainless steel electrodes assembled in coin cells (type: CR2032) in a glovebox under argon atmosphere. The measurements were carried out in a temperature range from -20 to 90 °C by varying the temperature in 5 or 10 °C steps. The sample was first conditioned at the target temperature for 60 min. In order to achieve accurate temperature control, the EIS measurement was not started before the temperature reached a constant temperature with a maximum deviation of 0.01 °C. For fitting the impedance data, the software ZView2 was used.

Additional information: The ion conductivity (σ) was calculated by using Eq. (S3),

$$\sigma = \frac{l}{R_b A} \tag{S3}$$

where l is the membrane thickness, A is the membrane area, and R_b is the bulk resistance of the SPE, which was obtained from the Nyquist plot.

Details of the annealing process: All SPEs show a sharp increase of the σ during the 1st heating cycle to 90 °C, in some cases by orders of magnitude. According to the $\vartheta_{g,PSy}$, which is in this temperature range (Table S2), this sudden increase can be attributed to the improved contact between the SPE membrane and both electrode surfaces. This short-term increase of σ cannot be explained by structural transformations of the BCP matrix, because they are taking place over longer periods of time at this temperature, as shown by a long-term SAXS measurement at 90 °C (Fig. S19a). Potentially, the briefly applied weak electric field during EIS measurement is sufficient to additionally align the Li^+ conduction pathways in direction of the electrode surfaces, because an applied electric field would lead the alignment in this direction.

During the further course of annealing, structural changes occur that can be divided into macroscopic and microscopic levels, whereby the respective effects can be mutually dependent and influence each other.

The macroscopic level relates to the morphology of the SPE. With increasing annealing duration and storage time at room temperature, a structural change occurs, as already described with respect to Fig. S19, and also possibly improved orientation and domain size.

The microscopic level refers to the common LiTFSI/PEO/THF microphase, where changes also seem to occur within. This is evident from a thin liquid film deposited outside the SPE membrane after

annealing, as shown in the photo in Fig. S20 of a SPE membrane sandwiched between two stainless steel electrodes that originated from an opened coin cell. This predominant THF loss leads increasingly to the stoichiometry between LiTFSI/PEO/THF in the microphase, which is required for the common crystal structure formation (Fig. 2b). Indeed, we observed this behavior in the WAXS curves for the SPE membranes stored at room temperature for a longer period of time, as more intense peaks appeared. In case that the appropriate stoichiometry is widely distributed, the crystalline domains percolate and form Li^+ conduction pathways, resulting in an exponential increase of the σ. Consequently, obtaining the crystal structure is critical to the formation of the observed superionic conductor with the cooperative conduction mechanism. However, in the absence of the appropriate stoichiometry or if only locally distributed, the crystalline structure is formed just in a part of the PEO domains, resulting in a lower σ, as it is the case at beginning of the annealing process.

Remarkably, in contrast to the case described by Zhou et al.[17] of decreasing σ during annealing, we observed a notable increase in σ despite the annealing process. This suggests that during the annealing process, in the LiTFSI/PEO/THF microphase, an appropriate stoichiometry for the formation of the crystal structure is provided due to the stabilization by the BCP matrix, wherein a minimum content of THF or solvent is strongly coordinated into the common crystal structure. Consequently, this prevents the LiTFSI from crystallization, because this would cause a sharp drop in conductivity, as it is an insulator.

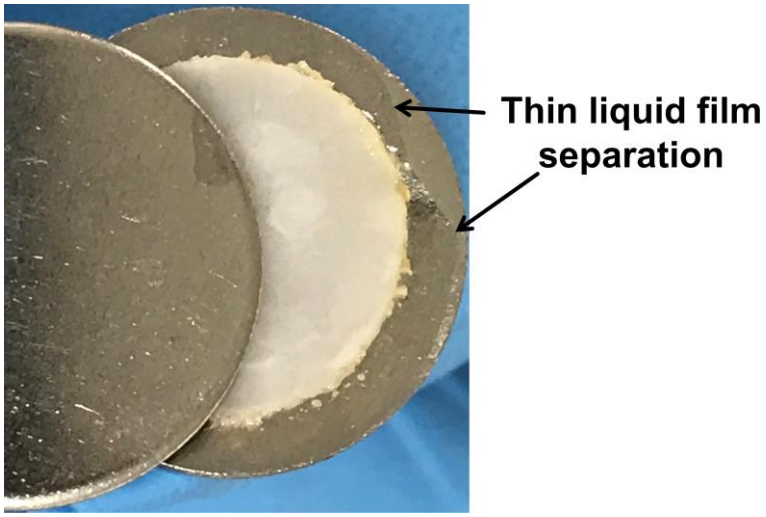

Fig. S20 | Thin liquid film deposition during SPE membrane annealing process. Photo of a SPE membrane sandwiched between two stainless steel electrodes, taken from an opened coin cell after the annealing process. The obtained predominant THF loss leads increasingly to the stoichiometry between LiTFSI/PEO/THF in the microphase, which is required for a common crystal structure, resulting in the percolation of the crystalline domains and the formation of Li^+ conduction pathways which are responsible for the extraordinary σ.

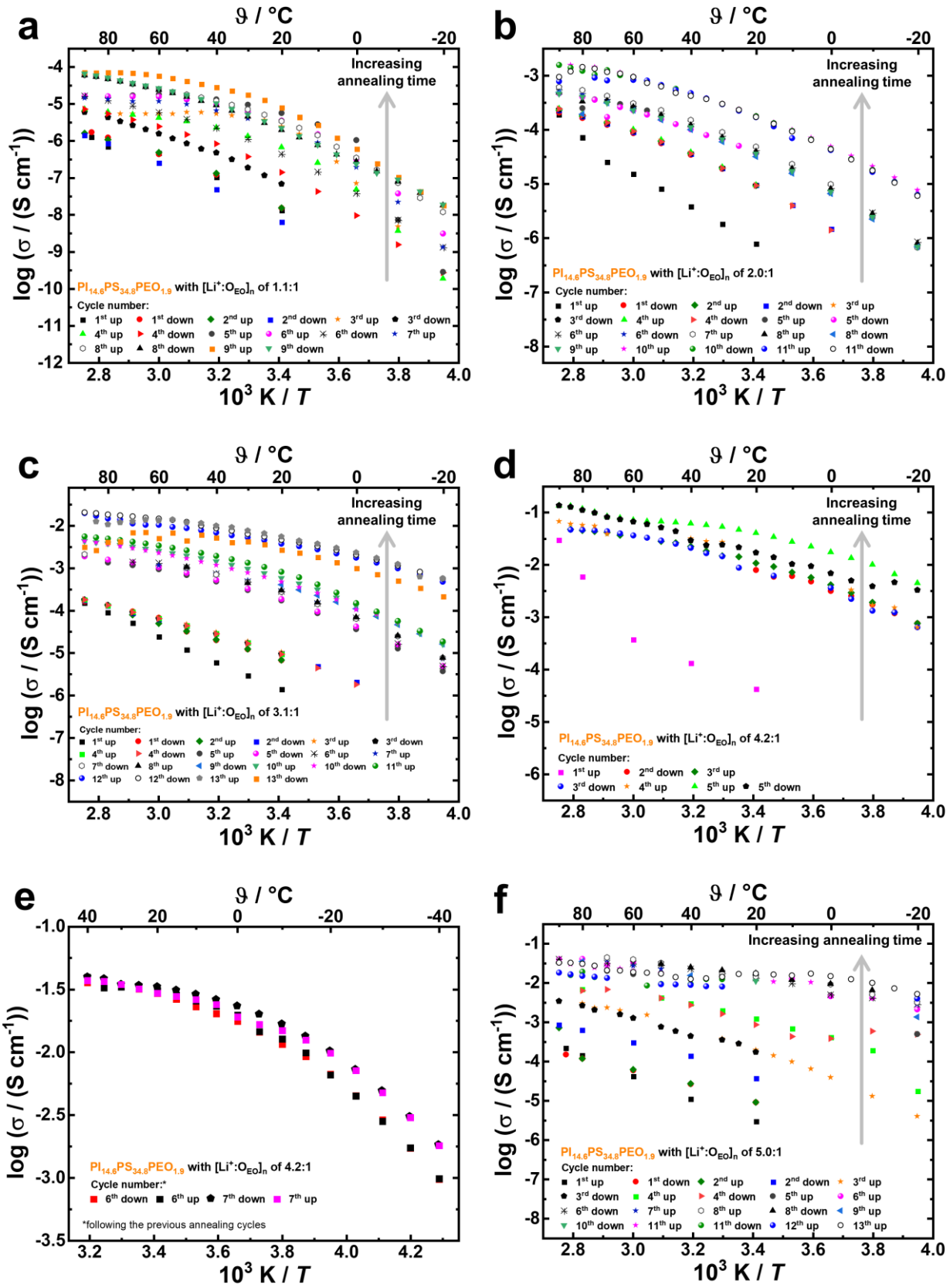

Fig. S21 | Arrhenius plot of the ionic conductivity (σ) change during the annealing process. By EIS measured σ from SPE membranes of LiTFSI/$PI_{14.6}PS_{34.8}PEO_{1.9}$/THF for a series of LiTFSI contents, increasing from $[Li^+:O_{EO}]_n$ = 1.1:1 to 5.0:1, in a temperature range from -20 to 90 °C are depicted. Note that in **e**, the σ to low temperatures of -40 to 40 °C is shown from the sample in **d**, after its annealing process. For reference, the standard LiTFSI/PEO electrolyte with $[Li^+:O_{EO}]$ = 0.1:1 is also plotted every time. In each case the cycle with the highest σ is additionally shown in Fig. 4a. With increasing duration of the annealing process, the σ increases considerably.

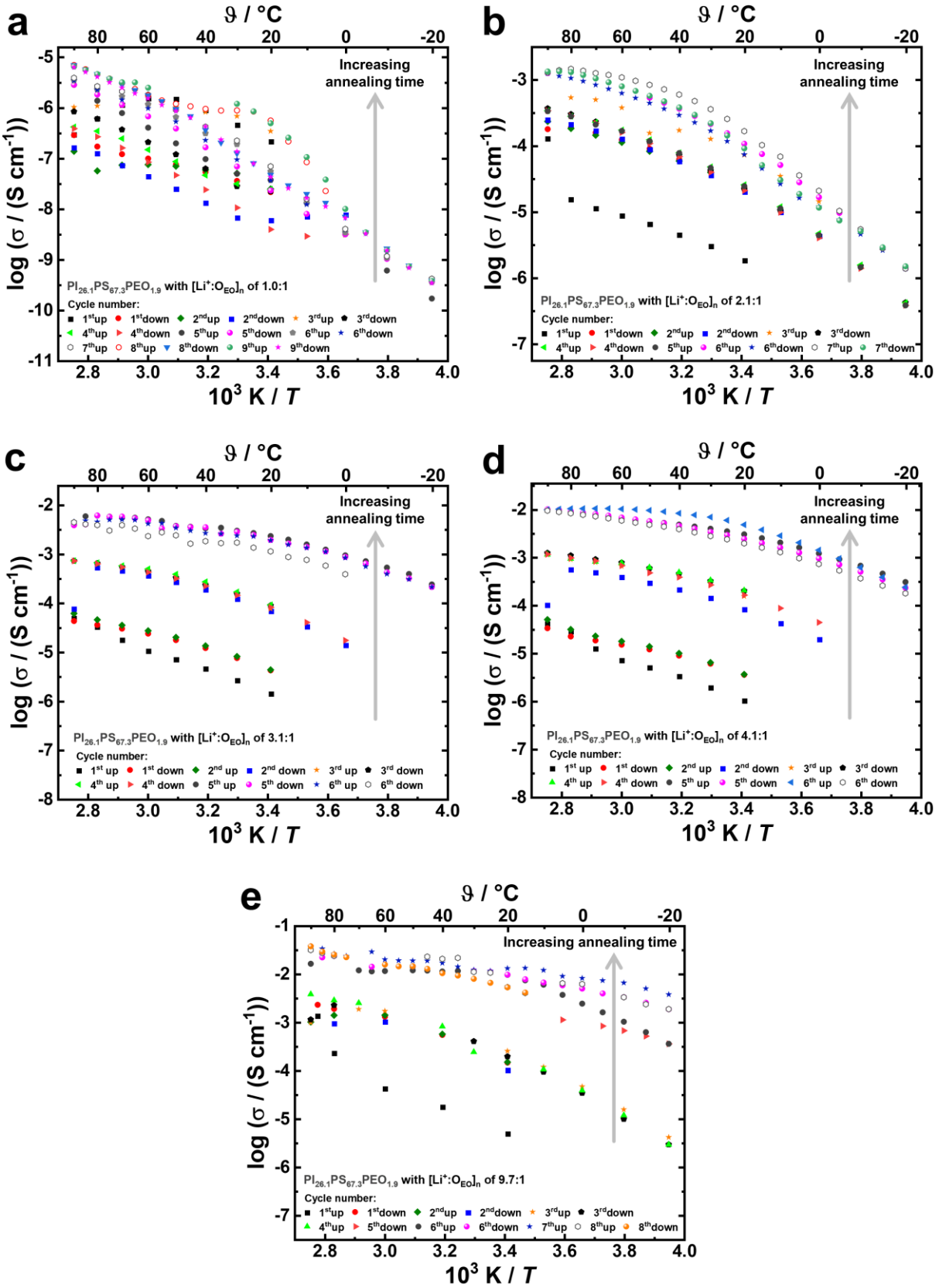

Fig. S22 | Arrhenius plot of the ionic conductivity (σ) change during the annealing process. By EIS measured σ from SPE membranes of LiTFSI/$PI_{26.1}PS_{67.3}PEO_{1.9}$/THF for a series of LiTFSI contents, increasing from $[Li^+:O_{EO}]_n$ = 1.0:1 to 9.7:1, in a temperature range from -20 - 90 °C are depicted. For reference, the standard LiTFSI/PEO electrolyte with $[Li^+:O_{EO}]$ = 0.1:1 is also plotted every time. In each case the cycle with the highest σ is additionally shown in Fig. 4b. With increasing duration of the annealing process, the σ increases considerably.

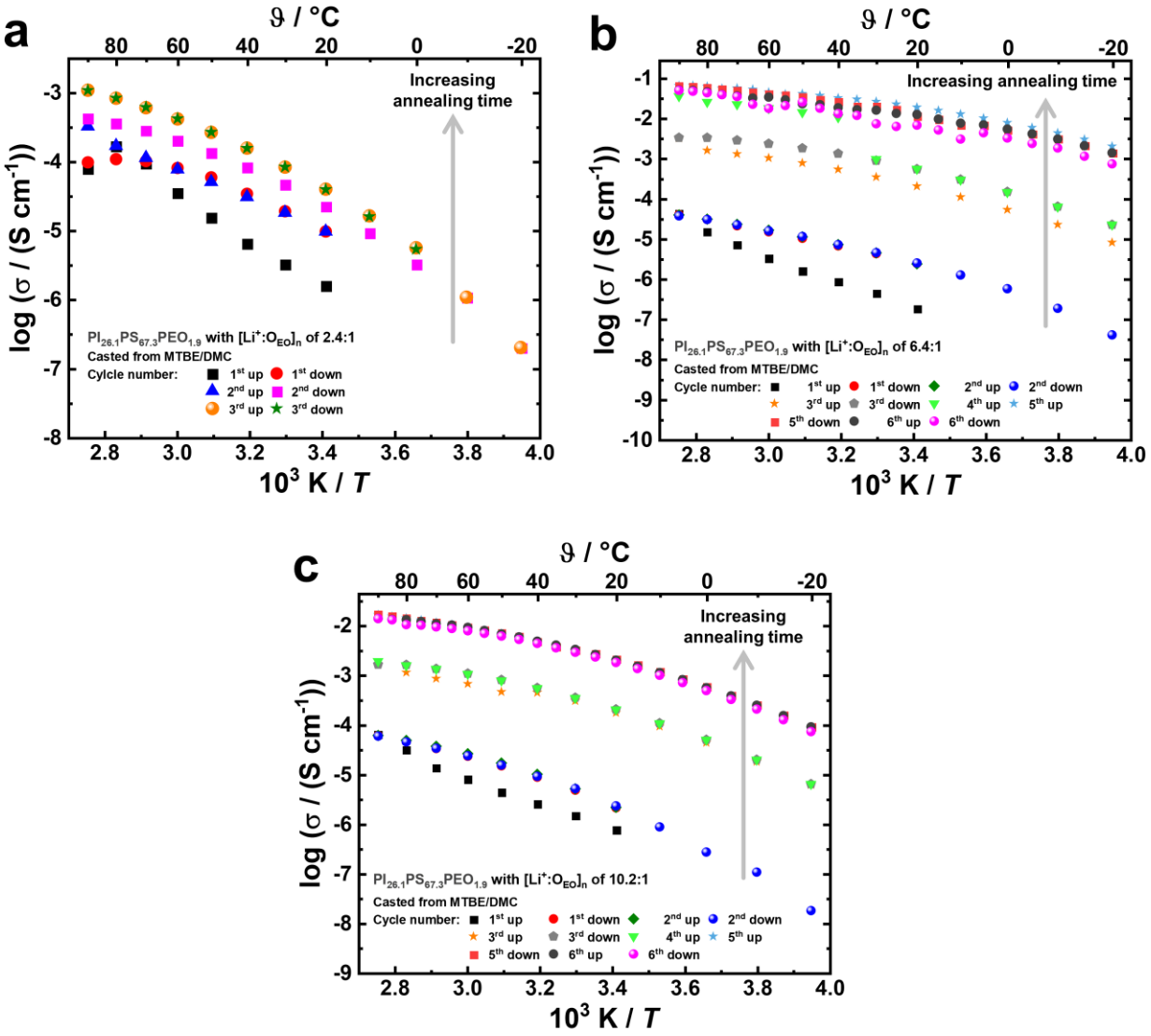

Fig. S23 | Arrhenius plot of the ionic conductivity (σ) change during the annealing process. By EIS measured σ from SPE membranes of LiTFSI/$PI_{26.1}PS_{67.3}PEO_{1.9}$/DMC for a series of LiTFSI contents, increasing from $[Li^+:O_{EO}]_n$ = 2.4:1 to 10.2:1, in a temperature range from -20 to 90 °C are depicted. For reference, the standard LiTFSI/PEO electrolyte with $[Li^+:O_{EO}]$ = 0.1:1 is also plotted every time. In each case the cycle with the highest σ is additionally shown in Fig. 4c. With increasing duration of the annealing process, the σ increases considerably.

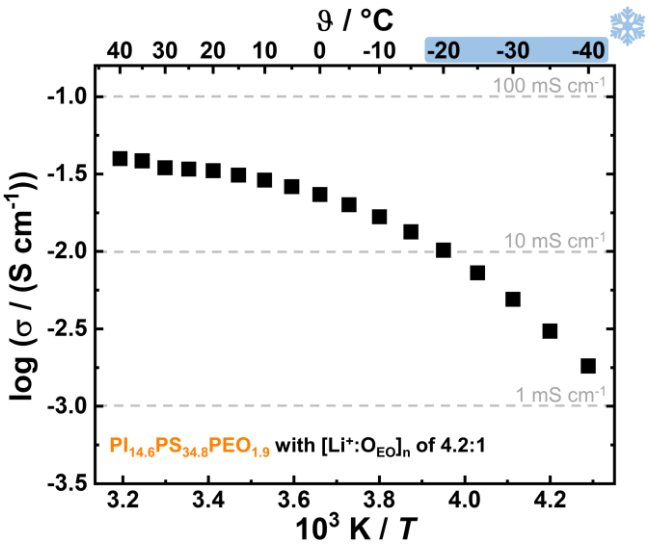

Fig. S24 | Arrhenius plot of the ionic conductivity (σ) for low temperatures down to -40 °C. By EIS measured σ from SPE membrane of LiTFSI/$PI_{14.6}PS_{34.8}PEO_{1.9}$/THF with a $[Li^+:O_{EO}]_n$ = 4.2:1 in a temperature range from -40 to 40 °C after the annealing process (Fig. S21d, e) are depicted. Noteworthy, a polymer-based electrolyte features σ in the range of $>10^{-3}$ S cm^{-1} even at temperatures down to -40 °C.

Table S5 | Activation energy (E_a) of all SPEs from both BCPs, and those casted from MTBE/DMC. E_a was obtained from the slope of the Arrhenius plot (ln(σ) vs. T^{-1}) of the σ values shown in Fig. 4 in the temperature range of 0 to 90 °C. Accordingly, the EIS measurement cycle with the highest σ obtained after annealing was used.

	LiTFSI/$PI_{14.6}PS_{34.8}PEO_{1.9}$/THF	0.0:1	1.1:1	2.0:1	3.1:1	4.2:1	5.0:1	-
$[Li^+:O_{EO}]_n$	**LiTFSI/$PI_{26.1}PS_{67.3}PEO_{1.9}$/THF**	0.0:1	1.0:1	2.1:1	3.1:1	4.1:1	5.2:1	9.7:1
	LiTFSI/$PI_{26.1}PS_{67.3}PEO_{1.9}$/DMC	-	-	2.4:1	-	-	6.4:1	10.2:1
		-	0.43	0.34	0.22	0.17	0.18 [a)]	-
	E_a / eV	-	1.14 [b)] / 0.38 [a)]	0.43 [c)]	0.17 [d)]	0.25 [e)]	-	0.13
		-	-	0.49	-	-	0.20	0.31

Determined in the temperature range of: 35 - 90 °C for [a)], 0 - 30 °C for [b)], 0 - 80 °C for [c)], 0 - 85 °C for [d)], and 0 - 60 °C for [e)].

DSC Measurements of SPEs from $PI_{26.1}PS_{67.3}PEO_{1.9}$ Casted from MTBE/DMC

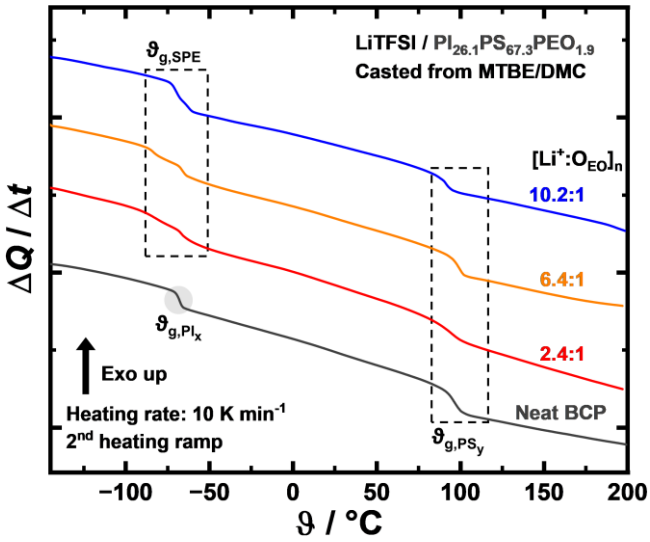

Fig. S25 | DSC measurements of SPEs from $PI_{26.1}PS_{67.3}PEO_{1.9}$ casted from MTBE/DMC depending on $[Li^+:O_{EO}]_n$ as well as the respective neat BCP. The simultaneous occurrence of the ϑ_g for the PS_y and PI_x blocks indicates that the BCP matrix of the SPE is microphase-separated. However, the ϑ_{g,PI_x} is overlapped by other signals, which together result in the $\vartheta_{g,SPE}$ (Fig. 1b).

Table S6 | Results of thermal analysis by DSC measurements of SPEs from $PI_{26.1}PS_{67.3}PEO_{1.9}$ casted from MTBE/DMC.

$[Li^+:O_{EO}]_n$	LiTFSI/$PI_{26.1}PS_{67.3}PEO_{1.9}$/DMC	0.0:1	2.4:1	6.4:1	10.2:1
	$\vartheta_{g,SPE}$ [a] / °C	-67.6 [b]	-67.1	-68.4	-67.3
	$\Delta C_{p,SPE}$ [a] / J (g K)$^{-1}$	0.136 [b]	0.178	0.189	0.193
	ϑ_{g,PS_y} / °C	95.8	95.0	98.6	91.2
	$\Delta C_{p,PS_y}$ / J (g K)$^{-1}$	0.205	0.174	0.158	0.140

[a] Consists of ϑ_{g,PI_x} and $\vartheta_{g,LiTFSI/PEO}$ signals and is additionally overlaid with the ϑ_g-signals of LiTFSI/PEO/DMC mixture. [b] Values only for the PI_x block from the neat $PI_{26.1}PS_{67.3}PEO_{1.9}$.

Calculation of LiTFSI Concentration in the LiTFSI/PEO/THF Microphase

Table S7 | LiTFSI concentration (c_{LiTFSI}) within the common LiTFSI/PEO/THF microphase. Calculated by relating the determined LiTFSI amount (Table 1) to the total volume fraction of the PEO phase (ϕ_{PEO}), where this is composed of the volume of LiTFSI, THF, and PEO (Table 1).

$[Li^+:O_{EO}]_n$								
	$PI_{14.6}PS_{34.8}PEO_{1.9}$	0.0:1	1.1:1	2.0:1	3.1:1	4.2:1	5.0:1	-
	$PI_{26.1}PS_{67.3}PEO_{1.9}$	0.0:1	1.0:1	2.1:1	3.1:1	4.1:1	5.2:1	9.7:1
c_{LiTFSI} / mol L^{-1}		-	3.7	4.1	4.2	4.2	4.1	-
		-	4.1	4.0	4.1	4.2	3.9	3.9

Spin Relaxation and Pulsed-Field-Gradient (PFG) NMR

Sample preparation: NMR tubes were filled with the SPE membrane in a drying room followed by sealing.

Measurement set-up: Observation time (Δ) dependent ^{7}Li- and ^{19}F-NMR pulsed-field-gradient (PFG)-NMR measurements were performed at constant temperature of 90 °C and Δ-range of 25 - 300 ms. Temperature-dependent ^{7}Li- and ^{19}F-NMR NMR spectra, PFG-NMR measurements and ^{7}Li spin-lattice relaxation measurements were performed over a temperature range of 0 to 90 °C, heating from 0 to 90 °C in 10 °C steps, holding at 90 °C for 10 hours with recording one measurement every hour, and then cooling down to 0 °C in 10 °C steps. In diffusion experiments the observation time was at Δ = 150 ms.

Additional information: A general error of 5% of the diffusion coefficients (D) is assumed.

Evaluation of spin relaxation data within the BPP model: The Bloembergen-Purcell-Pound (BPP) model [48] was used for the data analysis. Then, assuming isotropic rotational diffusion as the relevant motional mode, the spin-lattice relaxation rate R_1 at a Larmor frequency ω_0 can be described using Eq.(S4).

$$R_1 = \frac{1}{T_1} = A\left(\frac{\tau_c}{1+\omega_0^2\,\tau_c^2} + \frac{4\,\tau_c}{1+4\omega_0^2\,\tau_c^2}\right) \quad \text{(S4)}$$

Here, τ_c is the correlation time. For ^{7}Li the quadrupolar relaxation is the dominant mechanism leading to a prefactor A of the form

$$A_{\text{quad}} = \frac{3\pi}{10} \frac{2I+3}{I^2\,(2I-1)} \left(1+\frac{\eta}{3}\right) C_{\text{Q}}^2 \qquad \text{(S5)}$$

with I being the spin quantum number, η the asymmetry parameter of the electric field gradient and C_{Q} the quadrupolar coupling constant.

From Eq. (S4), the maximum of $R_1(\tau_c)$ occurs at a temperature T_{max}, where $\omega_0\,\tau_c = 0.616$. This allows calculation of τ_c at T_{max}, and subsequently the prefactor A is obtained. Finally, assuming Arrhenius behavior of τ_c, its temperature dependence and the activation energy of the local motion E_a can be derived according to Eq. (S6).

$$\tau_c = \tau_0\ \exp\left(\frac{E_a}{R\,T}\right) \qquad \text{(S6)}$$

Linewidth data are shown in Fig. S26. A comparison of the FWHM obtained from spectra with the homogeneous linewidth extracted from spin-spin relaxation rates indicates that the linewidths are dominated by heterogeneous broadening.

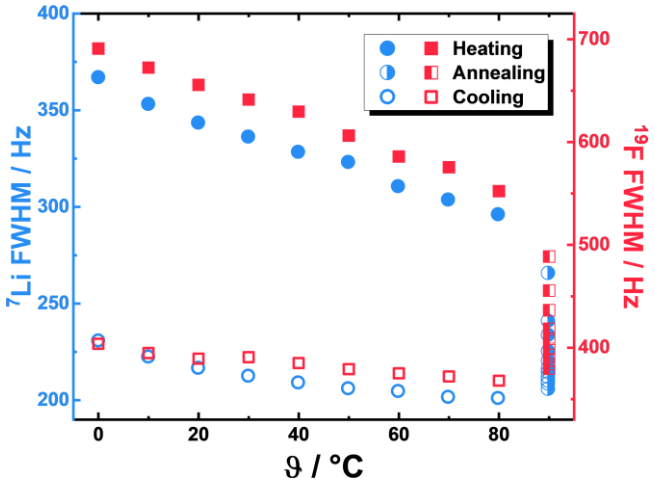

Fig. S26 | Temperature-dependent ^{7}Li and ^{19}F linewidths during a heating/cooling cycle. Spin relaxation NMR investigations in the temperature range from (0 - 90) °C for the SPE from LiTFSI/$PI_{14.6}PS_{34.8}PEO_{1.9}$/THF with $[Li^+{:}O_{EO}]_n$ = 4.2:1.

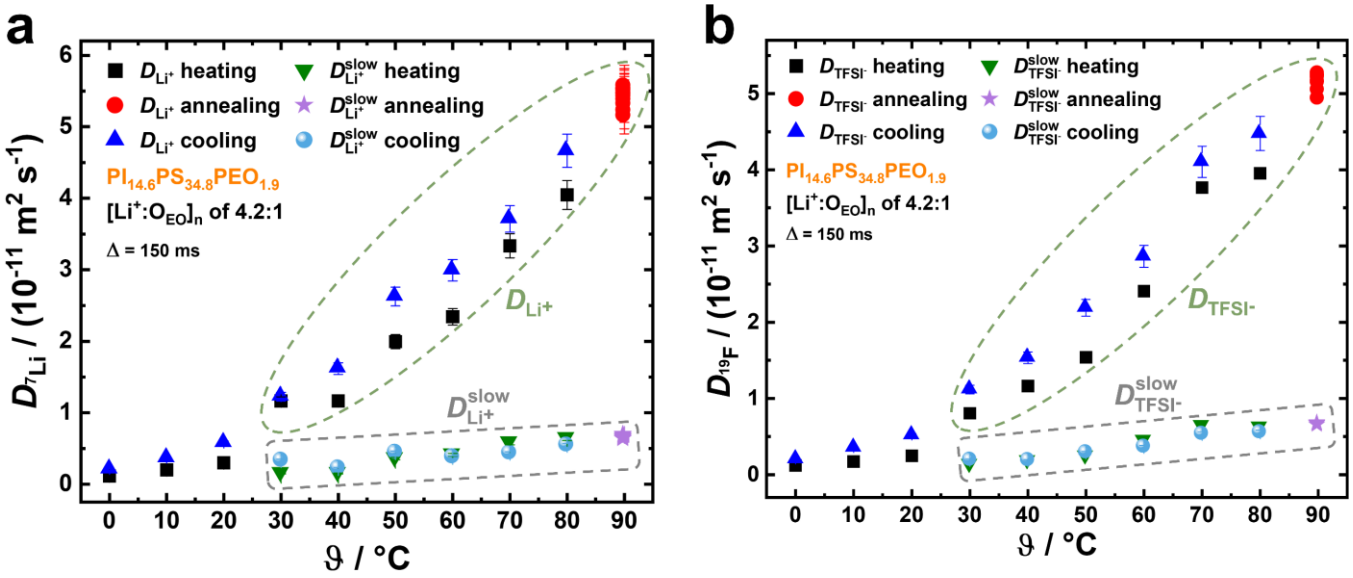

Fig. S27 | Temperature-dependent measurements of D_{Li^+} and D_{TFSI^-} to determine E_a. PFG-NMR results in **a**, for D_{Li^+} and in **b**, for D_{TFSI^-} performed on SPE of LiTFSI/$PI_{14.6}PS_{34.8}PEO_{1.9}$/THF with LiTFSI content of $[Li^+:O_{EO}]_n$ = 4.2:1. D_i^{slow} refers to a minor component (~30% of the intensity) with a slower diffusion.

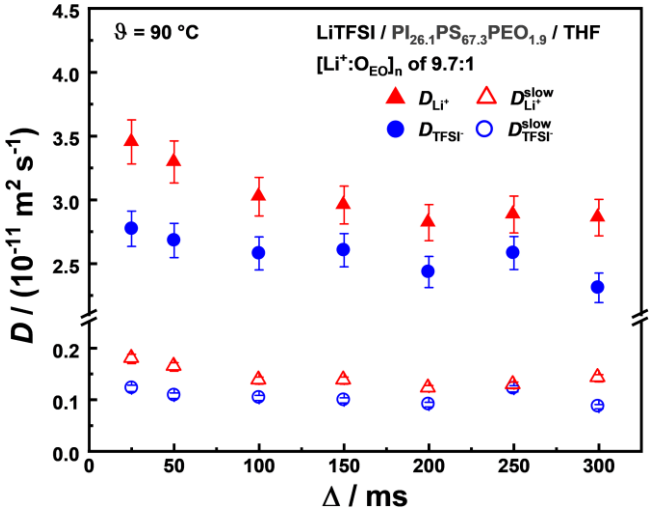

Fig. S28 | Observation time (Δ) influence on D_{Li^+} and D_{TFSI^-}. PFG-NMR results performed for SPE of LiTFSI/$PI_{26.1}PS_{67.3}PEO_{1.9}$/THF with LiTFSI content of $[Li^+:O_{EO}]_n$ = 9.7:1 after annealing at 90 °C, measured at 90 °C, in dependence of the observation time Δ.

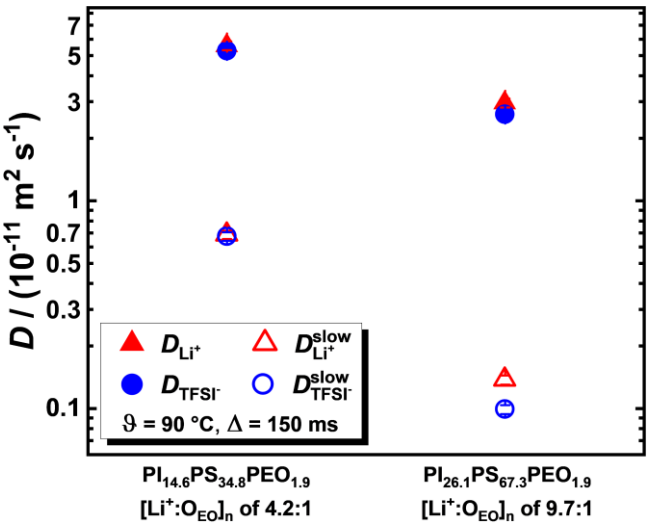

Fig. S29 | D_{Li^+} and D_{TFSI^-} of both investigated SPEs at 90 °C. PFG-NMR results performed on SPE of LiTFSI/$PI_{14.6}PS_{34.8}PEO_{1.9}$/THF with LiTFSI content of $[Li^+:O_{EO}]_n$ = 4.2:1 and for SPE of LiTFSI/$PI_{26.1}PS_{67.3}PEO_{1.9}$/THF with LiTFSI content of $[Li^+:O_{EO}]_n$ = 9.7:1 at an observation time (Δ) of 150 ms and at 90 °C.

Table S8 | Temperature-dependent PFG-NMR data. Diffusion coefficients (D_i), Li^+ transport numbers (T_{Li^+}) and the estimated limiting conductivities (σ_{lim}) for the fast and slow component measured after annealing at 90 °C during cooling from 90 °C to 0 °C in the SPE obtained from LiTFSI/$PI_{14.6}PS_{34.8}PEO_{1.9}$/THF with $[Li^+:O_{EO}]_n$ = 4.2:1.

Temperature / °C	D_{Li^+} [a] / $m^2\ s^{-1}$	D_{TFSI^-} [b] / $m^2\ s^{-1}$	σ_{lim} [c] / $S\ cm^{-1}$	T_{Li^+} [d]	$D^{slow}_{Li^+}$ [a] / $m^2\ s^{-1}$	$D^{slow}_{TFSI^-}$ [b] / $m^2\ s^{-1}$	σ^{slow}_{lim} [c] / $S\ cm^{-1}$	$T^{slow}_{Li^+}$ [d]
0	$2.0\cdot10^{-12}$	$2.0\cdot10^{-12}$	$7\cdot10^{-4}$	0.51	-	-	-	-
10	$3.6\cdot10^{-12}$	$3.5\cdot10^{-12}$	$1\cdot10^{-3}$	0.51	-	-	-	-
20	$5.7\cdot10^{-12}$	$5.1\cdot10^{-12}$	$2\cdot10^{-3}$	0.53	-	-	-	-
30	$1.2\cdot10^{-11}$	$1.1\cdot10^{-11}$	$4\cdot10^{-3}$	0.52	$3.3\cdot10^{-12}$	$1.9\cdot10^{-12}$	$8\cdot10^{-4}$	0.63
40	$1.6\cdot10^{-11}$	$1.5\cdot10^{-11}$	$5\cdot10^{-3}$	0.51	$2.2\cdot10^{-12}$	$1.9\cdot10^{-12}$	$6\cdot10^{-4}$	0.54
50	$2.6\cdot10^{-11}$	$2.2\cdot10^{-11}$	$7\cdot10^{-3}$	0.55	$4.4\cdot10^{-12}$	$2.9\cdot10^{-12}$	$1\cdot10^{-3}$	0.60
60	$3.0\cdot10^{-11}$	$2.9\cdot10^{-11}$	$8\cdot10^{-3}$	0.51	$4.1\cdot10^{-12}$	$4.5\cdot10^{-12}$	$1\cdot10^{-3}$	0.48
70	$3.7\cdot10^{-11}$	$4.1\cdot10^{-11}$	$1\cdot10^{-2}$	0.47	$5.8\cdot10^{-12}$	$6.4\cdot10^{-12}$	$2\cdot10^{-3}$	0.48
80	$4.7\cdot10^{-11}$	$4.5\cdot10^{-11}$	$1\cdot10^{-2}$	0.51	$6.4\cdot10^{-12}$	$6.2\cdot10^{-12}$	$2\cdot10^{-3}$	0.51
90	$5.6\cdot10^{-11}$	$5.3\cdot10^{-11}$	$1\cdot10^{-2}$	0.51	$6.9\cdot10^{-12}$	$6.7\cdot10^{-12}$	$2\cdot10^{-3}$	0.50

Values are plotted in Fig. S27a for [a] and in Fig. S27b for [b]. [c] To calculate, c_{LiTFSI} = 4.2 mol L^{-1} from Table S7, Eq. (3), and the respective *D*-values were used. [d] Calculated by Eq. (2) and using the respective *D*-values.

2D ^{1}H-^{1}H NMR Spectroscopy

We performed ^{1}H-^{1}H RFDR (Fig. S30) and ^{1}H-^{1}H NOESY NMR (Fig. S31) to investigate whether THF is present in the PI- and PS-microdomains.

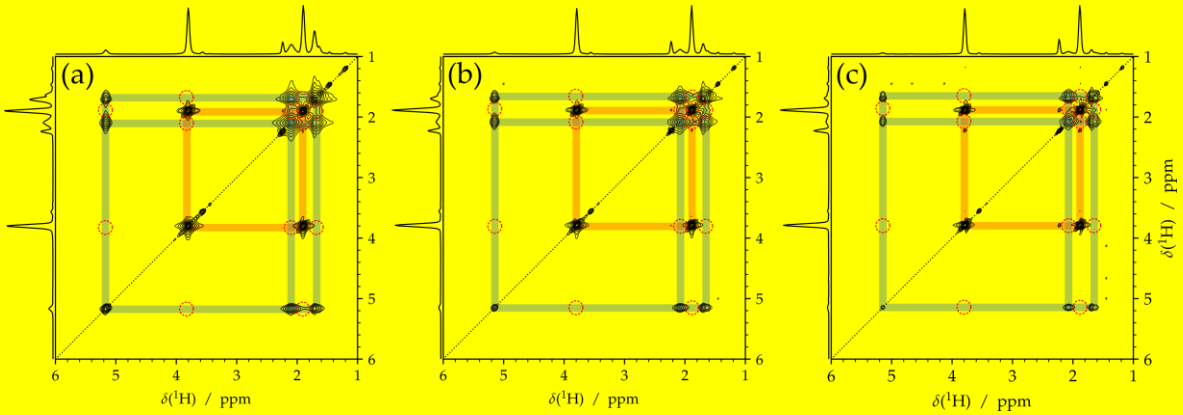

Fig. S30 | ^{1}H-^{1}H RFDR [S1] correlation spectra of the sample LiTFSI/$PI_{14.6}PS_{34.8}PEO_{1.9}$/THF with $[Li^{+}:O_{EO}]_n$ = 4.2:1 spinning at 5 kHz MAS (rotor period τ_{rot} = 200 µs) and B_0 = 11.74 T with varying recoupling times of (a) 51.2 ms (256 τ_{rot}), (b) 102.4 ms (512 τ_{rot}) and (c) 204.8 ms (1024 τ_{rot}). A train of rotor-synchronized 180° pulses with the XY16 phase scheme [S2] was used for dipolar recoupling and bracketed by two z-filter delays of 300 µs length. Quadratic sine apodization (QSINE with SSB = 3 in TopSpin) was used to increase the spectral resolution. 12 logarithmically distanced contour levels are drawn from 0.5 % to 95 % of the maximum intensity. All cross-correlation signals of the PI protons (marked with blue lines) are visible as well as those of the THF protons (marked with red lines). The red circles mark the expected positions of absent cross-correlation signals between PI and THF protons. Note that the PS proton resonances are not visible because of their much higher linewidth resulting from much shorter T_2 relaxation times because of the much lower mobility in the PS block compared to the PI and PEO blocks. This also renders presence of THF in the PS block unlikely as the solvent would increase the mobility to at least some extend. A correlation between THF and PS protons was also not detectable in ^{1}H-^{1}H DQ/SQ BaBa correlation spectroscopy (not shown).

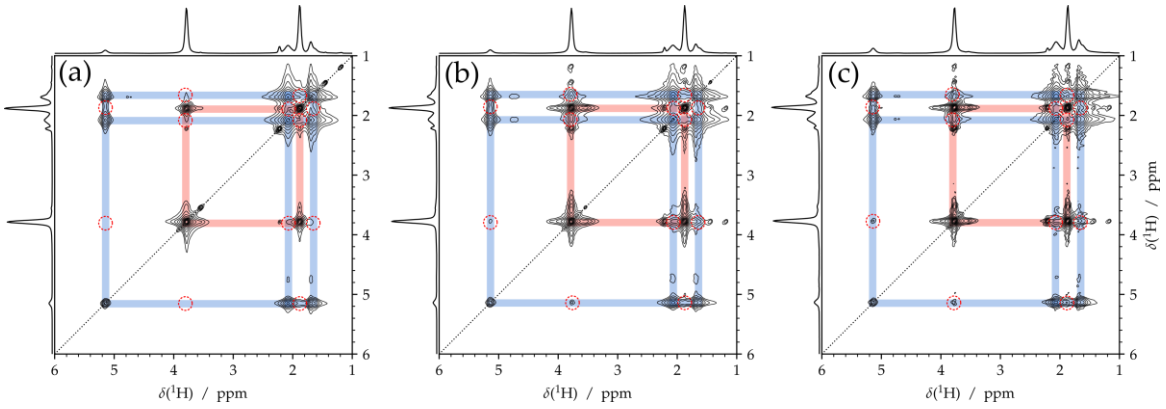

Fig. S31 | ^{1}H-^{1}H NOESY [S3] correlation spectra of LiTFSI/$PI_{14.6}PS_{34.8}PEO_{1.9}$/THF sample with $[Li^{+}:O_{EO}]_n$ = 4.2:1 spinning at 5 kHz MAS and B_0 = 11.74 T with varying mixing times of (a) 100 ms, (b) 500 ms and (c) 1.5 s. Longer mixing times to not give a sufficient signal-to-noise ratio due to the enhanced signal quenching by T_1 relaxation. Quadratic sine apodization (QSINE with SSB = 3 in

TopSpin) was used to increase the spectral resolution. 12 logarithmically distanced contour levels are drawn from 0.5 % to 95 % of the maximum intensity. All cross-correlation signals of the PI protons (marked with blue lines) are visible as well as those of the THF protons (marked with red lines). For the longer mixing times weak cross correlations appear between PI and THF protons which are, however, close to the limit of detection. From this it is concluded that THF is predominantly present in the PEO block and only small amount can diffuse in the PI block.

We observe that the ^{1}H-^{1}H-RFDR NMR spectra (Fig. S30) do not show cross-correlation signals between PI and THF protons. ^{1}H-^{1}H-NOESY NMR spectra (Fig. S31) show weak cross-correlations between PI and THF protons after long mixing times. This indicates that a very small fraction of THF, close to the NMR-detection limit, is localized in the PI-microdomains. The PS protons are not visible because of their much higher line width resulting from the low mobility of the PS chain segments. This indicates that no THF is present in the PS-microdomains, as otherwise the mobility would be noticeably increased. We therefore conclude, the performed ^{1}H-^{1}H-NOESY- and ^{1}H-^{1}H-RFDR-NMR indicate that THF is predominantly present in the PEO-microdomain.

Electrochemical Impedance Spectroscopy (EIS)

Fig. S31 shows the EIS-spectra of the best conducting LiTFSI/$PI_{14.6}PS_{34.8}PEO_{1.9}$/THF SPE for temperatures increasing from -40°C to 80°C.

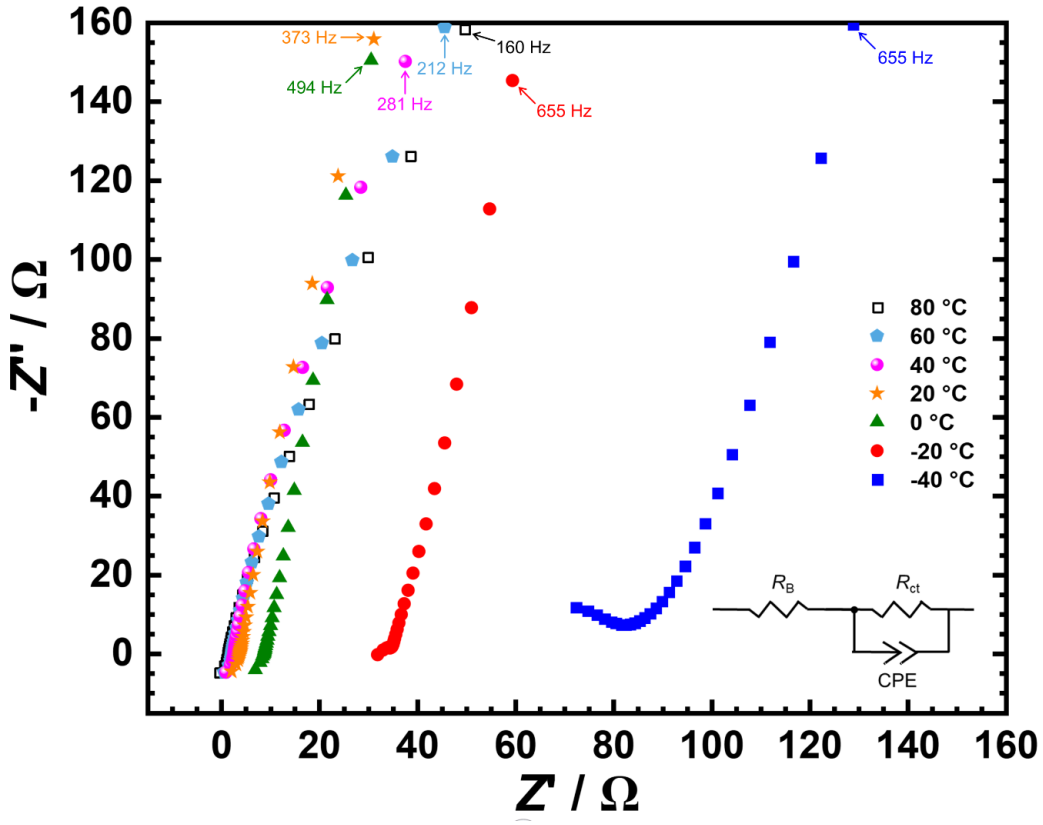

Fig. S32 | Fig. S32 | Nyquist plots determined by electrochemical impedance spectroscopy (EIS). Nyquist plots of the best conducting LiTFSI/$PI_{14.6}PS_{34.8}PEO_{1.9}$/THF sample with $[Li^+:O_{EO}]_n$ = 4.2:1 (Fig. S21, d), cycle no. 5 up) at temperatures increasing from -40°C to 80°C and measured in a frequency range from 1 MHz to 1 Hz with an electrode distance (sample thickness) of 0.044 cm and a contact area (sample area) of 0.283 cm^2. The enlarged range used for the analysis is shown, taking into account the frequency range of 1 MHz and the value shown in the figure, including the equivalent circuit diagram.

Electrochemical Stability Window (ESW)

Measurements of the electrochemical stability window for different SPE-solutions are shown in Figs. S33 and S34. For LiTFSI/$PI_{26.1}PS_{67.3}PEO_{1.9}$/THF we observe an electrochemical stability window of 0 – 4.1 V *vs.* Li|Li^+. The stability limit at 4.1 V is due to the oxidative electrochemical stability limit of THF. The PEO/DMC-mixture exhibits oxidative stability up to 5.1 V, indicating the potential to expand the stability limit into the range relevant for applications.

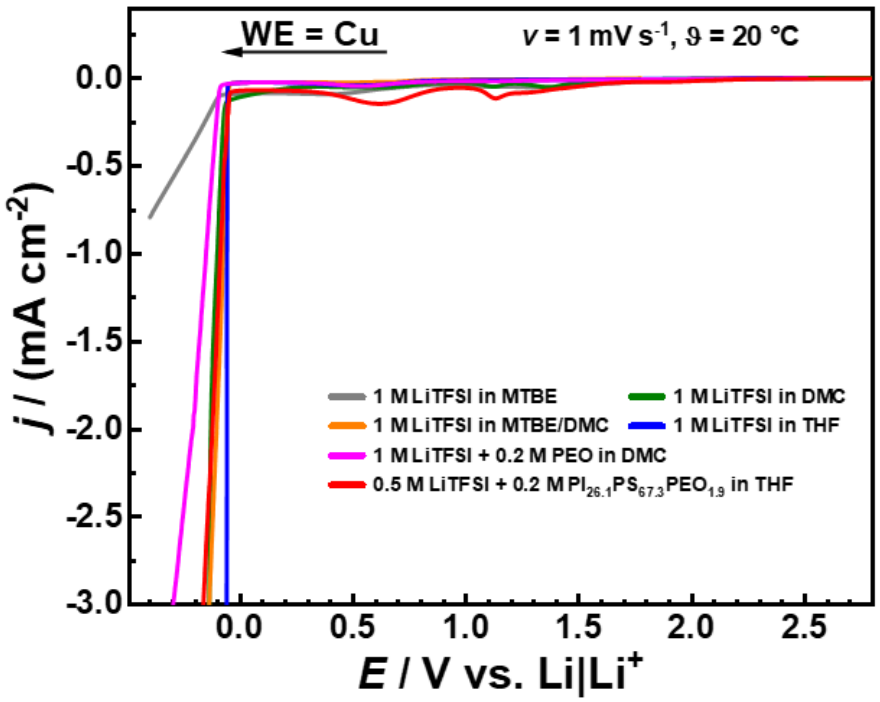

Fig. S33 | Electrochemical stability window for different LiTFSI/solvent/polymer combinations in solution. Reductive electrochemical stability of LiTFSI-mixtures with the solvents dimethylcarbonate (DMC), tetrahydrofuran (THF) and methyl-t-butyl ether (MTBE), and with PEO homopolymer and $PI_{26.1}PS_{67.3}PEO_{1.9}$.

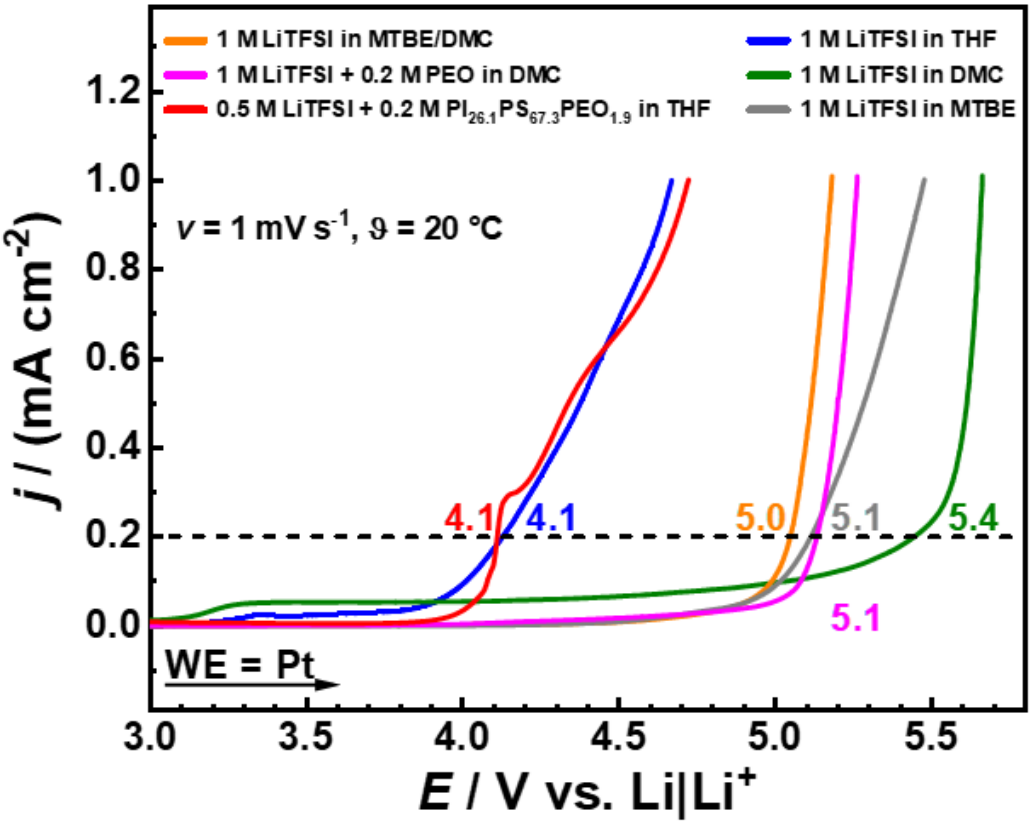

Fig. S34 | Electrochemical stability window for different LiTFSI/solvent/polymer combinations in solution. Oxidative electrochemical stability of LiTFSI-mixtures with the solvents dimethylcarbonate (DMC), tetrahydrofuran (THF) and methyl-t-butyl ether (MTBE), and with PEO homopolymer and $PI_{26.1}PS_{67.3}PEO_{1.9}$. For the LiTFSI/$PI_{26.1}PS_{67.3}PEO_{1.9}$/THF-mixture we observe the onset of oxidation at 4.1 V *vs*. Li|Li^+ due to the oxidative stability limit of the solvent THF. The measurements for DMC/PEO indicate the possibility to possibly extend the stability limit to 5.1 V *vs*. Li|Li^+.

References

S1. Nishiyama, Y., Zhang, R. & Ramamoorthy, A. *J. Magn. Reson.* **2014**, *243*, 25-32; doi 10.1016/j.jmr.2014.03.004.

S2. Gullion, T., Baker, D. B. & Conradi, M. S. J. Magn. Reson. 1969, 89, 479-484; doi 10.1016/0022-2364(90)90331-3

S3. Jeener, J., Meier, B. H., Bachmann, P. & Ernst, R. R. J. Chem. Phys. 1979, 71, 4546-4553; doi 10.1063/1.438208